Sea Breeze-Driven Daytime Vertical Distributions of Air Pollutants and Photochemical Implications in an Island Environment

Bohai Li[1], Shanshan Wang[1,2], Zhiwen Jiang[1], Yuhao Yan[1], Sanbao Zhang[1], Ruibin Xue[1], Yuhan Shi[1], Chuanqi Gu[1], Jian Xu[3], Bin Zhou[1,2,4]

[1]Shanghai Key Laboratory of Atmospheric Particle Pollution and Prevention (LAP[3]), Department of Environmental Science and Engineering, Fudan University, Shanghai, 200438, China.
[2]Institute of Eco-Chongming (IEC), Shanghai, 202162, China.
[3]National Space Science Center, Chinese Academy of Sciences, 100190 Beijing.
[4]Institute of Atmospheric Sciences, Fudan University, Shanghai, 200438, China.

Correspondence to: Shanshan Wang (shanshanwang@fudan.edu.cn)

Abstract. Atmospheric pollutants in island and coastal environments are profoundly modulated by sea breezes (SB) and typhoons. Understanding the characteristics of pollutants and their photochemical indicators under different airflow regimes is crucial for effective pollution control. Utilizing Multi-Axis Differential Optical Absorption Spectroscopy (MAX-DOAS) and a sea-land breeze objective identification algorithm, we reveal distinct spatiotemporal patterns in NO_2, HCHO, CHOCHO, and associated photochemistry under varying airflow patterns in a rural coastal area of Hainan. Non-sea breeze days (NSBDs) showed higher pollutant levels with broader vertical distribution range under conducive meteorological conditions. Conversely, on sea breeze days (SBDs), SB limits pollutant dispersion and its cooling effect suppresses ozone formation. Furthermore, SB also enhances transport of NO_2 and biogenic volatile organic compounds (BVOC) below 300 m, influencing ozone formation sensitivity (OFS) throughout SB phases. Typhoons effectively scavenge pollutants via strong winds and precipitation but also facilitate mid-to-high altitude BVOC transport and vertical dispersion of surface pollutants. Photochemical indicator analysis (HCHO/NO_2 [FNR] and CHOCHO/NO_2 [GNR]) indicates that the VOC-limited regimes persist even at high altitudes during typhoons. Elevated FNR and GNR thresholds suggest that existing OFS classifications are inadequate for low-NO_2 tropical coastal rural areas, underscoring the need for region-specific assessments. Given the BVOC-dominated environment and additional inputs from SB and typhoons, GNR proves more reliable than FNR for OFS determination. This study emphasizes the necessity of integrating local meteorology and environment conditions in O_3 control strategies, providing a scientific basis

for pollution mitigation in tropical coastal regions prone to SB and typhoons.

1 Introduction

Vertical gradients in atmospheric temperature, humidity, and solar radiation, among others, establish stratified photochemical environments, while atmospheric dynamics drive spatiotemporal heterogeneity in pollutant distribution, collectively rendering tropospheric chemistry evolution exceptionally complex (Jiang et al., 2008; Cooke et al., 2010; Wang et al., 2024; Gordon, 1987; Mason, 2013). As typical photochemical precursors, nitrogen dioxide (NO_2), formaldehyde (HCHO), and glyoxal (CHOCHO) exhibit unique vertical distributions in the troposphere. Vertical profiles of these species have been reported using gradient observations from various measurement techniques such as tethered balloons, unmanned aerial vehicles, towers, remote sensing techniques and aircraft (Glaser et al., 2003; Vo et al., 2018; Song et al., 2024; Chang et al., 2025; Wang et al., 2025; Benish et al., 2020). Among these, Multi-Axis Differential Optical Absorption Spectroscopy (MAX-DOAS) is a cost-effective, automated remote sensing technique capable of observing vertical changes in atmospheric trace gas concentrations over long periods of time. This method has been extensively applied worldwide for atmospheric composition monitoring (Wang et al., 2025; Wagner et al., 2011; Franco et al., 2015; Chang et al., 2025; Jiang et al., 2025).

NO_2 concentrations typically decrease exponentially with altitude due to it originates mainly from surface-level anthropogenic emissions, whereas photochemical oxidation of long-lived volatile organic compounds (VOCs) at high altitudes sometimes leads to higher distribution heights for HCHO and CHOCHO (Hong et al., 2022; Liu et al., 2023; Kumar et al., 2020). The ratio of CHOCHO to HCHO (R_{GF}) serves as a robust indicator for distinguishing VOCs sources due to their different sources and similar sinks (Zhang et al., 2021; Xing et al., 2020; Vrekoussis et al., 2010; Chan Miller et al., 2014). Observations reveal altitude-dependent characteristics of R_{GF}, with lower values at low altitudes reflecting dominant biogenic VOCs (BVOC) contributions, while elevated R_{GF} at higher altitudes highlights anthropogenic VOCs (AVOC) (Hong et al., 2022; Xing et al., 2020). The HCHO to NO_2 ratio (FNR) is widely used to assess O_3 formation sensitivity (OFS) by classifying regimes into VOC-limited, transition, and NO_x-limited regimes (Wang et al., 2025; Jiang et al., 2025; Liu et al., 2021). However, recent studies propose the CHOCHO as a more reliable indicator because it is more directly linked to secondary formation through the VOCs oxidation than HCHO (Hong et al., 2024; Liu et al., 2021). Therefore, comprehensive systematic investigation of

50 vertical distribution patterns of these species is critical for refining OFS assessments across atmospheric layers, optimizing

chemical transport models, and informing targeted air quality management strategies.

Coastal atmospheric environments are significantly influenced by sea-land breeze (SLB) circulation and typhoons. SLB, a

mesoscale phenomenon driven by thermal contrast, exhibits a diurnal alternation of onshore sea breezes (SB) and offshore

land breezes (LB), recirculating pollutants between marine and terrestrial zones (Zhao et al., 2022; Gangoiti et al., 2002;

55 Martins et al., 2012). SB enhances pollutant accumulation through reduced boundary layer height (BLH) and suppressed

vertical dispersion (Puygrenier et al., 2005), while its moisture influx alters temperature fields and photochemical conditions,

complicating secondary pollutant (e.g., ozone (O_3), secondary aerosols) distribution (Xu et al., 2021; Gangoiti et al., 2002).

Typhoons are large-scale weather systems that can cleanse pollutants via strong winds and precipitation (Yang et al., 2012;

Roux et al., 2020), yet their peripheral subsidence zones with reduced cloud cover intensify solar radiation, triggering severe

60 surface ozone pollution (Wu et al., 2013; Deng et al., 2019). Additionally, typhoon-enhanced winds promote cross-regional

O_3 transport (Wang et al., 2024; Qu et al., 2021). Both air currents critically modulate pollutant vertical structures and

photochemical environments across atmospheric layers Nevertheless, research gaps persist regarding vertical distributions of

NO_2, HCHO, and CHOCHO under SB and typhoon conditions, particularly in island.

Hainan Island is located far from mainland China and adjacent to the South China Sea, where its favorable topography and

65 geographic position render it frequently influenced by SB and typhoons (Zhang et al., 2014; Liang and Wang, 2017; Fu et al.,

2023). Given the superior air quality—mean NO_2 (7.34 μg m^3) and O_3 (52.80 μg m^3) concentrations below the National

Ambient Air Quality Standard (NAAQS) Grade II and urban VOCs (13.1 ppbv) remaining significantly lower than megacities

like Beijing and Shanghai—it has earned designation as a National Ecological Civilization Pilot Zone of China (Xu et al.,

2024; Yu et al., 2024). Notably, several studies have shown that typhoons and the East Asian monsoon can transport pollutants

70 such as O_3 and its precursors to the island via regional-scale advection, thereby inducing pollution events (Zhan et al., 2023;

Fu et al., 2023; Xu et al., 2024). However, the specific effects of SB and typhoons on O_3 precursors over Hainan Island are

still unclear.

By combining ground-based MAX-DOAS measurement with meteorological reanalysis data, we investigated the

spatiotemporal distributions of NO_2, HCHO, CHOCHO, and their photochemical indicators under various air current patterns

75   (ACPs) in the coastal area of Hainan. This study aims to elucidate the transport mechanisms of pollutants in complex

atmospheric environments and their response characteristics to local photochemical processes, thereby supporting air pollution

control and environmental management in coastal regions.

2 Data and Methods

2.1 Measurement of trace gases profile

80   This study was conducted in Hainan National Field Science Observation and Research Observatory for Space Weather

(19.53°N, 109.14°E) at Fuke village (FK), Danzhou City, Hainan Province, during the summer of 2024 (June 1 to August 31).

The observation site (Altitude approx. 100 m) lies within a topographically complex region bordered to the northwest by the

Beibu Gulf and to the southeast by the Wuzhi Mountain massif (18.9°N, 109.7°E) (Fig. 1a). During the observation period,

the observation site was directly affected due to the passage of Typhoon "Prapiroon" from south-east to north-west across

85   Hainan Island. The national expressway G98 passes about 1,600 m north-west of FK (Fig. 1b). The MAX-DOAS instrument

comprises a scanning telescope, a stepper motor controlling the zenith observation angle, an Ocean Optics QE65 Pro

spectrometer, and a data processing computer (Fig. 1c). Data acquisition is conducted daily from 06:00 to 19:00 local time

(LT), with dark current signals automatically extracted from nightly background measurements.

Spectral data were analyzed using the QDOAS software (http://uv-vis.aeronomie.be/software/QDOAS/), which retrieves

90   differential slant column densities (DSCD) of trace gases by fitting their characteristic absorption bands with reference cross-

sections and background corrections. Both ultraviolet (UV) and visible (VIS) channels were employed for oxygen dime (O_4),

NO_2, HCHO and CHOCHO DSCD retrievals, with configurations detailed in Table S1. Zenith spectra during each scan cycle

served as Fraunhofer reference spectra (FRS) to roughly eliminate stratospheric contributions. Measured spectra underwent

minor shift and stretch corrections to mitigate instrument instability effects. Quality control excluded retrievals with RMS >

95   0.001 or DSCD error to DSCD ratios exceeding 10% (30% for HCHO, 50% for CHOCHO). Observations before 07:00 and

after 18:00 were excluded due to insufficient light intensity. Detection limits (DDL) for different elevation angles were

calculated following S1 (Supplements). NO_2 data all exceeded DDL, while HCHO and CHOCHO exhibited significant

proportions of sub-DDL values (particularly CHOCHO at high elevations), attributable to their low concentration levels. To preserve temporal continuity, sub-DDL results were retained rather than discarded in subsequent analyses. Typical DOAS

100 fitting results for four gases are illustrated in Fig. S1.

This study employed the HEIPRO algorithm (Heidelberg Profile, developed by IUP Heidelberg) based on optimal estimation methodology (OEM) to retrieve vertical profiles of tropospheric trace gases (Frieß et al., 2006; 2011). The algorithm incorporates the SCIATRAN radiative transfer model (RTM) as an orthorectification mode (Rozanov et al., 2002). The retrieval strategy comprises two sequential steps: (1) aerosol extinction vertical profiles are derived from measured O_4 DSCD,

105 followed by (2) trace gas profile retrievals using the aerosol profiles as inputs in RTM. Vertical grids for trace gases span 0.0–3.0 km altitude with 100 m resolution, and retrievals were performed at 10-minute intervals. Exponential decay functions served as a priori profiles for all species with error S_a of 100% and 500 m covariance correlation length. Fixed aerosol parameters included: 0.3 km^{-1} extinction coefficient, 0.1 surface albedo, 0.95 single scattering albedo, and 0.72 asymmetry parameter at 360 nm (Henyey and Greenstein, 1941; Zhang et al., 2021). Surface concentrations of NO_2, HCHO, and

110 CHOCHO were initialized at 2, 5, and 0.2 ppbv, respectively. Representative retrieved profiles are illustrated in Fig. S2. To ensure that further analyses were based on reliable data, the absolute deviation thresholds between measured and modelled DSCD (optical densities, OD) values were set to 1×10^{-3}, 2×10^{15}, 7×10^{15} and 4×10^{14} molec cm^{-2} for O_4 OD, NO_2, HCHO and CHOCHO DSCD, respectively, in addition to retaining only those results with a degree of freedom of the signal (DoF) > 1.0. Filtered data showed strong model-measurement agreement (R^2 > 0.95), confirming retrieval accuracy (Fig. S3).

115 In addition, hourly surface O_3 mass concentrations (μg m^3) at the reference state (298 K, 1,013 hPa) were recorded at the DongPo School monitoring station (DPS, 19.52°N, 109.56°E) using a Thermo Scientific 49i O_3 analyzer were converted to surface VMRs (ppbv) for the analysis of photochemical indictors.
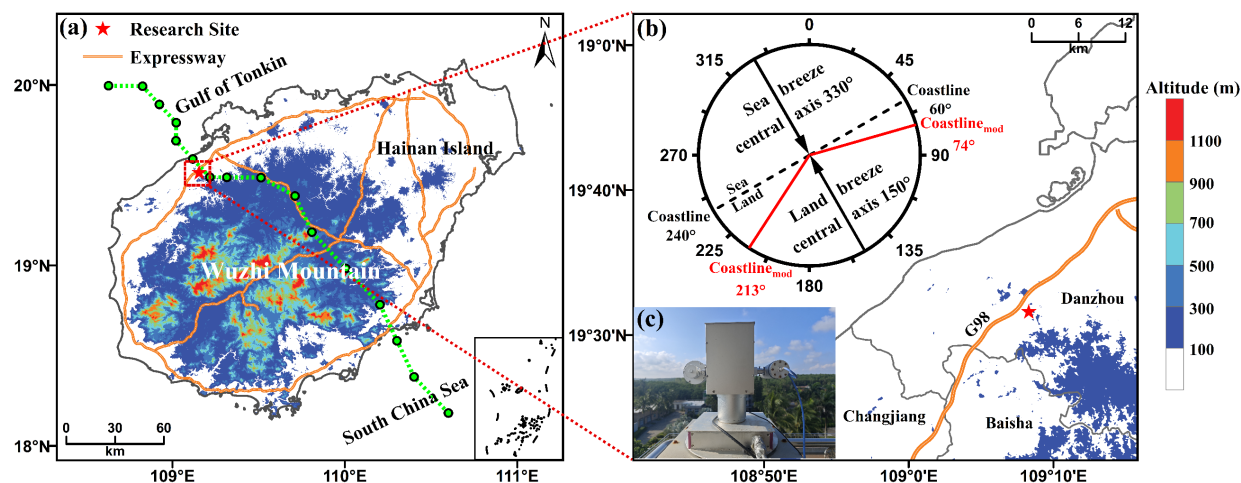
Figure 1. Overview of the study area and MAX-DOAS. (a) Topographic map of the area around the geopotential height and Multi-Axis Differential Optical Absorption Spectroscopy (MAX-DOAS) measurement station (19.53°N, 109.14°E) in Hainan Province, marked by a red five-pointed star, and the highway network is indicated by a yellow line. The track of the typhoon "Prapiroon" is shown by the green dotted line; (b) Topographic map of the area around the observation site, where a highway (G98) passes about 1,600 m to the northwest of the observation site. Compass charts for recording the direction of the sea breezes (SB) and land breezes (LB) are given in the upper left. The central axes of the SB and LB directions are shown by black arrows, and the red solid lines represent the modified coastline (Coastline_{mod}); and (c) MAX-DOAS instrument.

2.2 Identification of sea and non-sea breeze days

In this study, a filtering method was adopted as the primary means of identifying days favorable to SB development. Although this approach may underestimate SB frequency, the results will not be ambiguous. Accurate identification of onshore and offshore WD is essential for the method's effectiveness, with the geometry of the coastline serving as the basis for determining the central axes of SB and LB (Azorin-Molina et al., 2009; Azorin-Molina et al., 2011; KiranKumar et al., 2019). Accurate determination of onshore and offshore WD is critical to the identification process, and the orientation of the local coastline serves as the basis for defining the principal axes of SB and LB. In the vicinity of FK, the coastline at larger scales is approximately linear, extending from 240° to 60°, with the central axes of the SB and LB oriented at 321° and 141°, respectively (Fig. 1a,b). However, previous studies have shown that local coastline geometry and topographic influences, in combination with coastal-parallel flows driven by the Coriolis force, can induce deviations in the SB direction (Azorin-Molina et al., 2011; Miller et al., 2003). Based on these local features, the directional range of the SB at FK was revised to span from

213° to 74° (The red solid lines on the compass map in Figure 1b). In addition, islands and peninsulas can trigger SB fronts along different segments of the coastline (Zhu et al., 2017), whereas mountainous terrain often inhibits inland propagation (Barthlott and Kirshbaum, 2013). Specifically, on Hainan Island, the central Wuzhishan mountain range acts as a barrier to the

140 southeastward SB front, limiting its reach into the FK. Notably, during summer, the island is predominantly influenced by the southwesterly monsoon, which frequently produces daytime background winds oriented landward or along the coast. The formation pattern of these background air currents is fundamentally different from that of the SB. To enhance the contrast with sea breeze days (SBDs), dates influenced by background winds or failing to meet the SB criteria were identified. Those with anomalously elevated daytime relative humidity were excluded to minimize the influence of marine air masses. The remaining

145 dates were classified as non-sea breeze days (NSBDs).

Figure S4 illustrates the flow of an objective recognition algorithm (ORA) for SLB containing four modules and 12 filters. Unless otherwise noted, the data used by ORA are near-surface data. Module 1 filters the large-scale circulation background unfavorable to the formation of SLB, one of the important factors influencing the formation of SLB, through the wind speed (WS) and direction (WD) at high altitude (filters 1 to 2) (Arrillaga et al., 2020). Module 2 is the core module, which contains

150 three channels: channels 1 (filter 3 to 7-1) and 2 (filter 3 to 7-2) are based on the sudden change of WS and WD to identify the SB, and the rate of change of WS is introduced to capture the dynamics of the local wind field (filter 5-2), which can make up for the deficiencies of the traditional WS thresholding method; channel 3 rejects dates potentially affected by oceanic currents by setting a relative humidity (RH) increase threshold (filters 8-9). Module 3 excludes large-scale airflow disturbances through barometric pressure conditions (filters 10-11). Module 4 ensures that the remaining days satisfy the minimum sea-land

155 temperature gradient (filter 12) as a prerequisite for SB establishment. The specific functions of the modules and filters are detailed in S2 (Supplements).

2.3 Meteorological reanalysis data

Meteorological data were obtained from the European Centre for Medium-Range Weather Forecasts (ECMWF) fifth-generation atmospheric reanalysis product (ERA5), incorporating three principal components: the ERA5 single-level dataset,

160 ERA5 pressure-level data, and ERA5-Land. The single-level dataset provides hourly surface and sea-level parameters at 0.25°

spatial resolution, while the pressure-level product delivers three-dimensional atmospheric profiles across 37 vertical levels

from 1,000 hPa to 1 hPa, maintaining equivalent spatial and temporal resolutions. The ERA5-Land component—released in

2019—offers enhanced terrestrial monitoring through refined 9 km spatial resolution while preserving hourly temporal

sampling. Specific meteorological variables employed in this analysis, along with their respective dataset sources are

165   comprehensively detailed in Table S3. Notably, ERA5 lacks the surface RH data required; therefore, we computed actual and

saturated water vapor pressures using the 2m dew temperature and 2m temperature from ERA5-Land, respectively, and derived

RH from their ratio.

3 Results

3.1 Time Series of the Measurement Results

170   Figure 2 presents the time series daily near-surface aerosol extinction coefficient (AEC), NO_2, HCHO, CHOCHO volume

mixing ratios (VMRs), corresponding column integrated aerosol optical depth (AOD) and vertical column densities (VCDs)

observed by MAX-DOAS at FK, Hainan Island, China during the 2024 summer season (1 June–31 August). The measurements

reveal distinct atmospheric characteristics shaped by regional environmental conditions. Summer aerosol loading exhibited

markedly lower values compared to urban agglomerations like Beijing and Shanghai (where AOD typically exceeds 0.5), with

175   mean AEC and AOD measuring 0.11 ± 0.03 km^{-1} and 0.29 ± 0.1, respectively (Cheng et al., 2015; Zheng et al., 2019). The

average NO_2 surface VMRs (1.61 ± 0.53 ppbv) was 3 to 5 times lower than values recorded in Chinese megacity centers (Lou

et al., 2025), reflecting minimal local traffic and industrial emissions. Notably, HCHO and CHOCHO concentrations reached

levels comparable to metropolitan regions such as Beijing (HCHO surface VMRs: 4.41 ppbv) and Guangzhou (CHOCHO

surface VMRs: 0.13 ppbv) (Hong et al., 2024). This likely stems from biogenic emissions from surrounding tropical

180   ecosystems compensating for diminished anthropogenic sources.

In refined temporal resolution (Fig. S6). HCHO and CHOCHO exhibited significant positive correlations with elevated

temperatures (> 30°C) and reduced humidity (< 60%), particularly during two enhanced photochemical periods: 12–22 June

and 1–23 August, when the elevated concentrations persisted from the surface through elevated atmospheric layers. Surface

VMRs and VCDs show relatively similar patterns in their time series for all species because of their predominantly low-level distribution. However, during specific episodes (e.g., August 7–10, 2024), pronounced fluctuations in vertical temperature and humidity profiles resulted in a clear decoupling between surface and column measurements for NO_2, HCHO, and CHOCHO, which was more pronounced in aerosols. This suggests that the vertical distribution pattern of pollutants may involve more complex physicochemical processes that deserve further investigation.
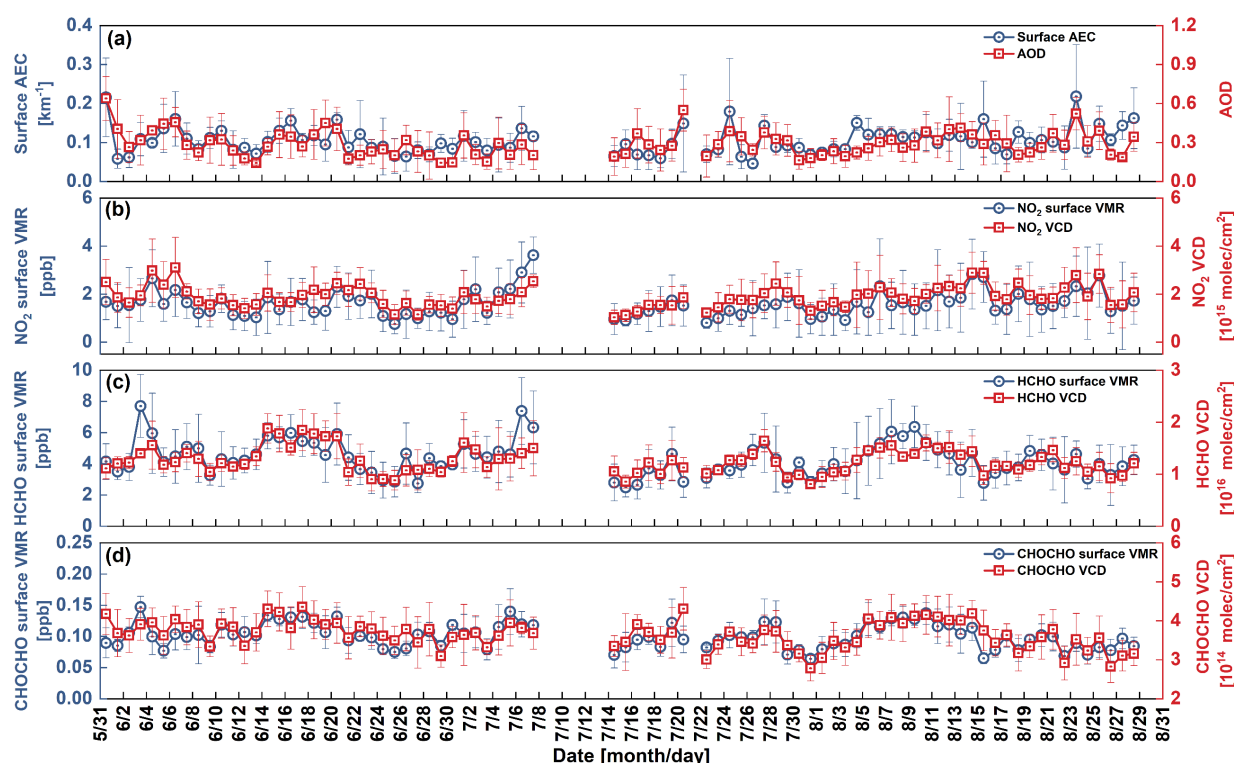
Figure 2. Diurnal variation of pollutants at FK. Time series of daily (a) aerosol, (b) NO_2, (c) HCHO and (d) CHOCHO surface mixing ratios and vertical column densities from MAX-DOAS measurements in Hainan Island, China.

Figure 3 illustrates the average diurnal variation and daily profiles of aerosol, NO_2, HCHO, CHOCHO, temperature and RH during the campaign. Aerosols, HCHO, and CHOCHO exhibited vertical distribution patterns that closely tracked the diurnal variation of BLH. Their vertical distributions peaked synchronously with maximum BLH at noon, followed by gradual subsidence to lower altitudes during afternoon planetary boundary layer (PBL) contraction, though residual amounts persisted in upper layers. The peak of the AEC occurs at the top of the boundary layer almost throughout the observing period due to

the aerosols from different sources consistently suppressing the daytime PBL (Xin et al., 2023). Notably, the aerosol vertical distribution bears a remarkable similarity to the RH, with a corresponding humidity maximum observed simultaneously at the top of the PBL throughout the diurnal cycle. This phenomenon reflects aerosol hygroscopic growth characteristics, particularly the water vapor sensitivity of fine particulate matter, which enhances light extinction at these altitudes (Liu et al., 2020). The occasional observed deviation between surface AEC and total AOD variations (Fig. 2a) may also be explained by this altitude-dependent hygroscopic behavior.

The diurnal NO_2 cycle exhibited a characteristic bimodal pattern, with primary peaks in morning (08:00 LT, VMRs = 2.67 ppbv) and evening (17:00 LT, VMRs = 1.66 ppbv) aligned with traffic rush hours, reflecting dominant vehicular emission sources. Notably, a secondary minor peak emerged at 14:00 LT, potentially driven by regional transport mediated by local circulation patterns (e.g., SB systems) (Fig. 6b). Vertically, NO_2 predominantly resides below 300 m. The early peaks of HCHO and CHOCHO are attributed to the oxidation of residual VOCs by OH radicals in the previous night and the rerelease from the aerosols (Xing et al., 2020; Liu and Wang, 2024). In contrast, the delayed HCHO peak (10:00 LT, VMRs = 5.14 ppbv) suggests the existence of additional emission sources beyond this mechanism, which are likely linked to morning traffic emissions. CHOCHO surface VMRs (0.12 ppbv) exhibited a distinct peak between 12:00–13:00 LT, potentially linked to photooxidation of VOCs—particularly alkenes and aromatics—and elevated temperatures that intensified photochemical activity and biogenic isoprene emissions (Duncan et al., 2010; Hendrick et al., 2014). However, A slow decreasing trend regarding the HCHO surface VMRs was still detected in the concurrent period, most likely due to the stronger vertical convection after midday, transferring the secondary HCHO production to higher altitudes (< 800 m) and thus diluting the surface concentration. In contrast, CHOCHO has a shorter atmospheric residence time (~1.3 h) and thus remains confined to lower altitudes (< 500 m) (Wittrock et al., 2006; Zhang et al., 2025). The late afternoon rebound in HCHO and CHOCHO concentrations may be due to reduced atmospheric mixing and lower photolysis rates as temperatures drop and solar radiation decreases (Chauhan et al., 2025).
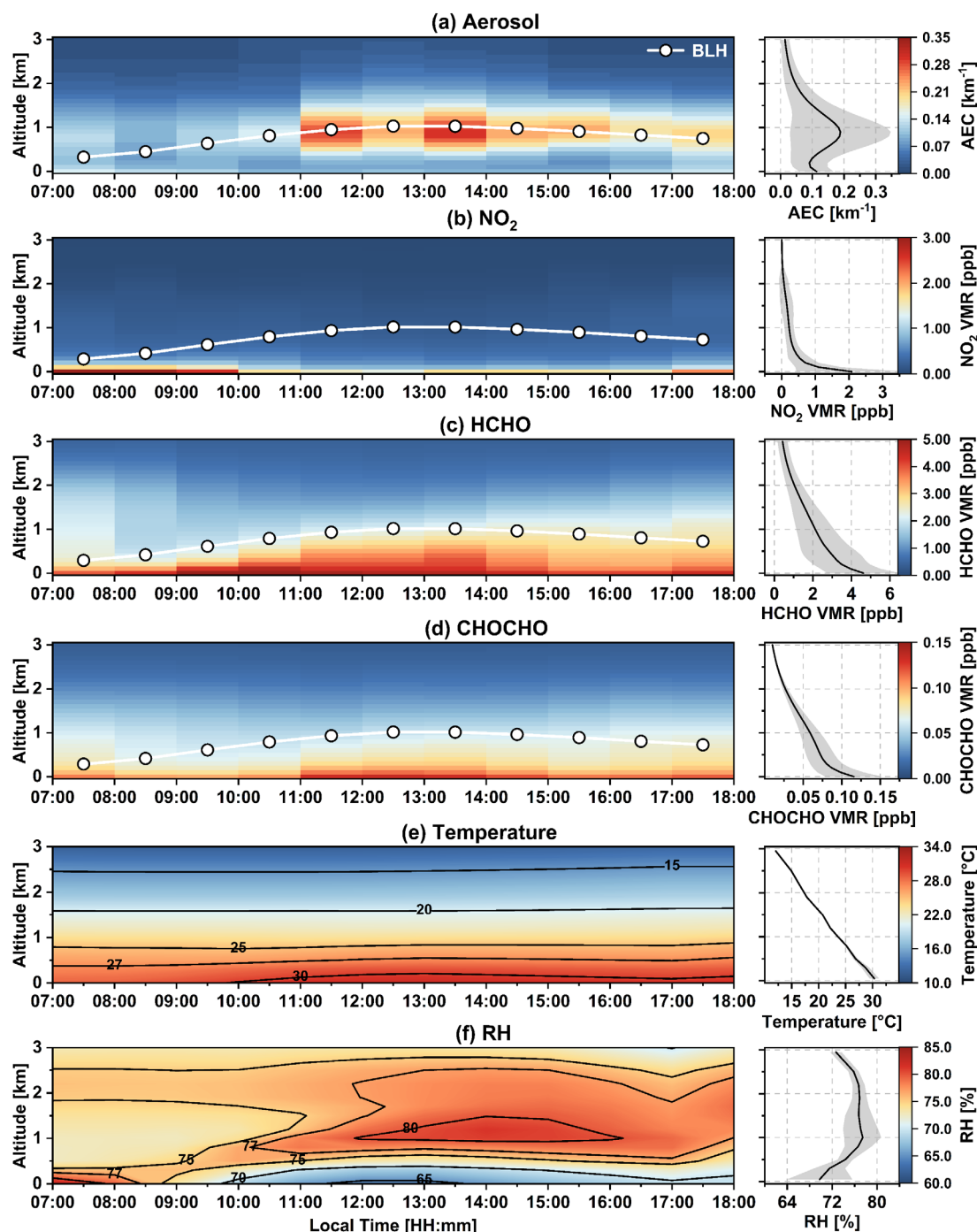
Figure 3. Diurnal variations in vertical profiles of pollutants and meteorological factors at FK. (a) AEC, (b) NO₂, (c) HCHO, and (d) CHOCHO measured by MAX-DOAS; (e) Temperature and (f) relative humidity (RH) from ERA5 reanalysis. Boundary layer height (BLH) cycles are indicated, while mean vertical profiles displayed in right panels.

3.2 Air current patterns impacted meteorological parameters and trace gases

During the campaign, Typhoon "Prapiroon" traversed Hainan from southeast to northwest on July 21–23, 2024, and its intense

225   disturbances to the local meteorology continued for one week after landfall (Fig. 1a and 5). We treated these seven Typhoon

days (TDs) as an independent case against NSBDs and SBDs identified by the ORA (Table S4). Days influenced by synoptic-

scale systems or hybrid weather patterns were excluded to ensure sample representativeness. Notably, most of the SBDs occur

consecutively, reflecting the regularity of the local mesoscale circulation. Figure 4 presents the occurrence frequency of

NSBDs, SBDs, and TDs, as well as the frequency distribution of SB onset and cessation times (O_{time} and C_{time}). The frequency

230   of NSBDs and SBDs was 32 days (34.8% of the total observation period) and 31 days (33.7%), respectively. The study site

exhibited 6.3% lower SB frequency compared to Hainan's regional average (Zhang et al., 2014). SB initiation predominantly

occurred after 10:00 LT, peaking at 10:00–13:00 LT (n = 21), likely driven by rapid solar heating in late morning (Parker,

2015). Cessation events clustered post-sunset, with a maximum occurrence at 18:00 LT (n = 16), consistent with the restoration

of thermal equilibrium following land surface cooling.

235
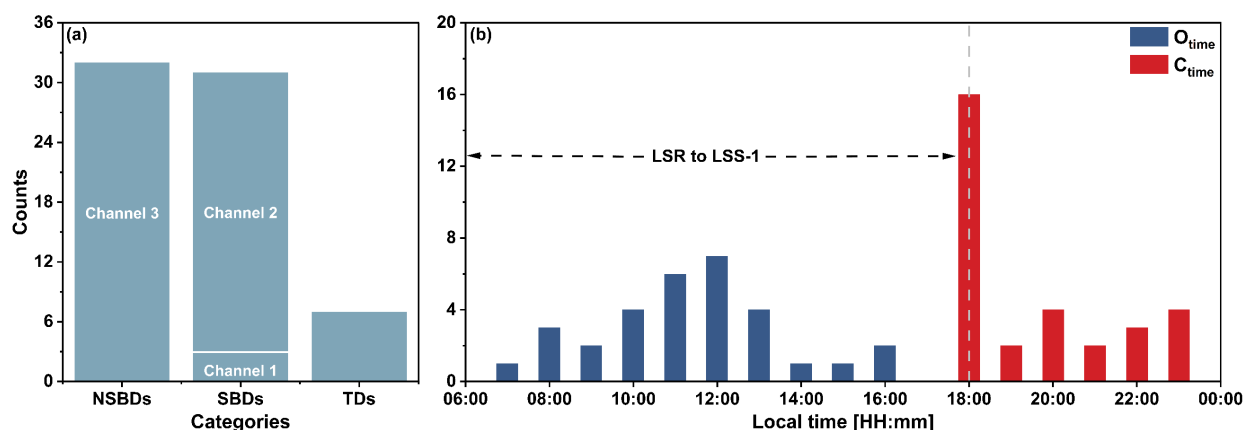
Figure 4. Statistics of the results of objective recognition algorithm for different air currents. (a) the frequency of occurrence of NSBDs, SBDs and TDs, as well as (b) the frequency distribution of SB onset and cessation times (O_{time} and C_{time}). The time ranges for local sunrise (LSR) and one hour before local sunset (LSS) are marked with dotted arrows.

Afterwards, the mean diurnal variations of each meteorological parameter: WS, WD, temperature, RH, BLH, and UV radiation

240   flux (UVF) in three ACPs are summarized in Figure 4. It should be noted that the composite analysis of SBDs excludes dates

selected through Channel 1 methodology due to systematic discrepancies in meteorological characteristics compared to

Channel 2-derived selections (Fig. S7). This exclusion is maintained in all subsequent analyses unless otherwise specified. Typhoon events show higher WS than NSBDs, but their diurnal variations are similar. Southwesterly winds persist under the typhoon's peripheral airflow, whereas NSBDs feature daytime southwest winds shifting to southerly at night. The weaker WS

245 of SB (peak 1.89 m s^{-1} at 14:00 LT) likely results from urban/vegetation friction and climate impacts of warming and urbanization (Fu et al., 2011; Guo et al., 2011; Li et al., 2018). Observational data reveal a distinct diurnal cycle in SBDs: after sunrise, WS decreased markedly until reaching a trough at 10:00 LT, followed the WD veered from southeast (149.7°) to south-southeast (170.3°), indicating dissipation of the onshore winds. SB onset at 11:00 LT brought a 41.3° clockwise shift to southwest and rising WS. Maximum SB intensity occurred at 15:00 LT with northwesterly flow (289.3°), then winds gradually

250 weakened and shifted offshore. A sharp transition (17:00–18:00 LT) featured a 97.2° anticyclonic shift from southwest (222.3°) to southeast (125.0°), with minimal wind speed (0.37 m s^{-1}), signaling SB termination and LB onset.

Compared to SB and typhoon conditions, NSBDs exhibit higher surface temperatures and UVF coefficients, likely attributable to reduced cloud cover and enhanced solar irradiance. The well-documented SB thermal mitigation effect manifests itself in the transport of water vapor inland by advancing oceanic breeze fronts (Yan and Anthes, 1988), producing discernible surface

255 cooling and driving a premature rise and anomalous increase in RH following the SB onset (13:00–17:00 LT) (Fig. 5c,d). Typhoon conditions exhibit thermal minimums due to combined radiative shielding from cyclonic circulation and extensive cloud coverage, while maintaining elevated humidity levels (mean RH: 82.28 ± 3.49%) through continuous moisture advection. BLH displays distinct variability across ACPs: NSBDs show rapid BLH growth peaking at 1,215.72 m (13:00 LT) from enhanced thermal convection, whereas TDs achieve the highest mean BLH (694.07 ± 122.07 m) through persistent vertical

260 wind shear and turbulent mixing (NSBDs: 619.26 ± 363.76 m, SBDs: 385.31 ± 281.80 m). Consistent with previous findings, SB conditions exhibit suppressed PBL development, attributable to periodic advection of stable marine air masses that inhibit atmospheric destabilization (Puygrenier et al., 2005; Li et al., 2025).
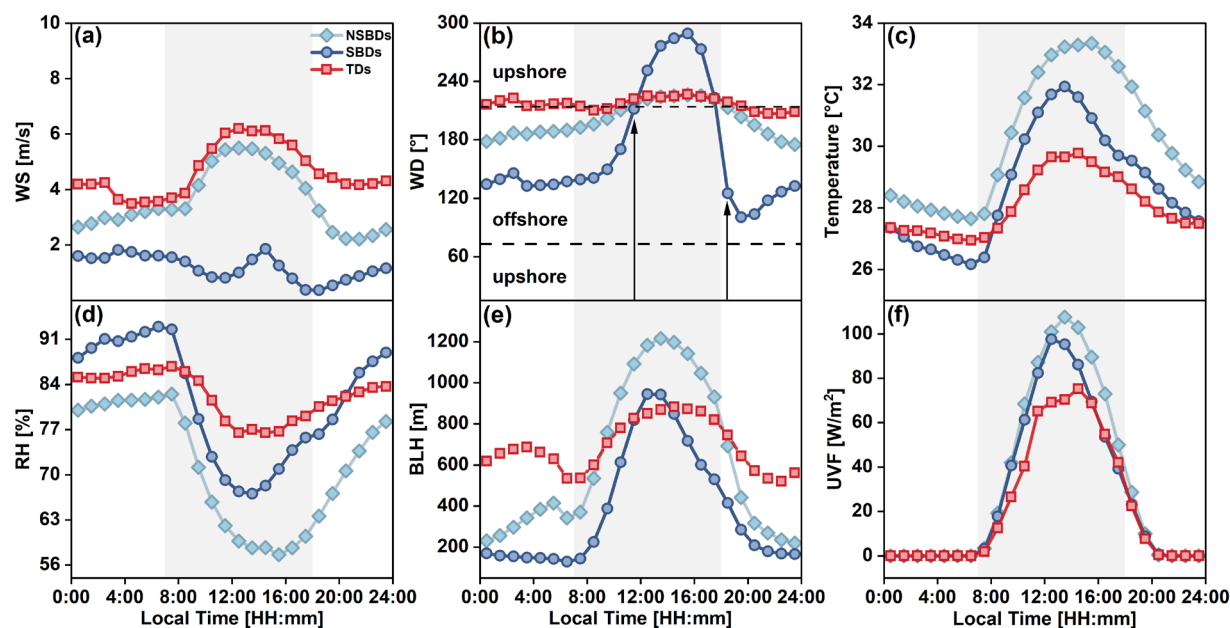
Figure 5. Diurnal variations of meteorological factors under different air currents. Mean diurnal variations of (a) WS, (b) WD, (c) temperature, (d) RH, (e) BLH, and (f) UV radiation flux (UVF) under three air current patterns (ACPs): NSBDs, SBDs, and TDs. The gray shaded area represents observation period of MAX-DOAS. The two black dotted lines define the range of WD for onshore and offshore winds. Critical transition points for SB initiation and cessation are marked with arrows in (b).

Accompanied with meteorological parameters, it can be expected that the vertical distribution of NO_2, HCHO and CHOCHO would be also varied under different ACPs. As shown in Fig. 6, surface NO_2 exhibit typical bimodal diurnal variations (morning/evening peaks) during both NSBDs and TDs, which is contrast to the distinct NO_2 accumulation pattern with concentrations rising sharply from 12:00 LT, peaking at 15:00 LT (2.10 ppbv) during SBDs, temporally coupled with SB front progression. There was a 69.6% increase in NO_2 throughout, which results in the SBDs (1.73 ± 0.30 ppbv) exhibiting the largest mean surface VMRs compared to the NSBDs (1.52 ± 0.82 ppbv) and TDs (1.23 ± 0.59 ppbv). This synchronisation suggests that pollutants from the onshore WD (particularly the northwest and northeast) are transported locally by the SB and accumulate due to the weak WS (Fig. S8). HCHO and CHOCHO average surface concentrations exhibited similar gradient patterns along with ACPs: NSBDs (HCHO: 4.84 ± 0.67 ppbv, CHOCHO: 0.114 ± 0.017 ppbv) > SBDs (HCHO: 4.26 ± 0.75 ppbv, CHOCHO: 0.108 ± 0.017 ppbv) > TDs (HCHO: 3.74 ± 0.52 ppbv, CHOCHO: 0.0995 ± 0.010 ppbv), which is closely related to the differences in their meteorological factors (WS, temperature, RH and UVF) (Fig. 5). Diurnal profiles of surface

HCHO and CHOCHO on NSBDs and TDs were consistent with their average patterns throughout the summer. In contrast,

280   SBDs induce a unique bimodal HCHO distribution with primary (5.10 ppbv) and secondary (5.08 ppbv) maxima at 10:00 and

13:00 LT. CHOCHO peaks occurred at 12:00 LT (0.15 ppbv) on NSBDs but shifted to 13:00 LT (0.13 ppbv) on SBDs. This

delayed peak is temporally synchronized with the secondary peak of HCHO, suggesting that the SB transports VOCs to the

local area, whose photo-oxidation further affects the HCHO and CHOCHO concentrations at FK. J. Wang et al. (2025)

similarly found that SB brings in air masses from boats, vegetation, and marine organisms, resulting in high levels of carbonyls

285   in coastal areas in the spring.

Vertical profiling analysis reveals distinct stratification characteristics of pollutants across three ACPs. For NO_2, maximum

concentrations remain consistently confined below 300 m altitude across all patterns. It is important to note that the horizontal

transport of the SB results in overall higher NO_2 concentrations within 0-300m after the O_{time} (Fig. 6b). Similar to the surface

concentrations, the vertical gradients of HCHO and CHOCHO followed NSBDs > SBDs > TDs sequence, clustering at

290   800/500/300 m and 400 m/300 m/surface, respectively. Thermodynamic vertical transport mechanisms significantly influence

pollutant distribution. Intense midday thermal plume convection causes HCHO and CHOCHO to disperse upward. As

temperatures drop, convective activity decreases, but residual pollutants remain at higher altitudes and continue vertical

transport through atmospheric motions. During marine breeze episodes, the thermal internal boundary layer (TIBL, ~200 m

thick) forms as cold marine air flows over the warm land surface, restricting pollutant dispersion (Arrillaga et al., 2016; Cuxart

295   et al., 2014; Talbot et al., 2007). Observations revealed that pollutant concentrations were significantly elevated within the

TIBL during SB penetration, with CHOCHO being particularly persistent. Interestingly, the WD at altitudes above 500 m

shifted to southerly after 15:00 LT on SBDs, which weakened pollutant transport and subsequently led to significant reductions

in NO_2, HCHO, and CHOCHO concentrations at elevated levels, especially HCHO (Fig. 6f and S9).

Surface VMRs to VCDs ratios (R_{SV}), quantifying altitudinal distribution patterns (Fig. 6d,h,i). Elevated R_{SV} values indicate

300   enhanced near-surface accumulation, whereas lower values suggest predominant vertical dispersion to higher altitudes.

Following SB incursion, the universal elevation of R_{SV} across species suggests that the onshore winds primarily affect

pollutants in the lower atmosphere. Notably, the significantly more pronounced R_{SV} enhancement observed in CHOCHO

relative to HCHO suggests that marine-transported VOCs prefer to produce CHOCHO rather than HCHO. In addition, the

average R_{SV} (NO$_2$: 0.71 ± 0.090; HCHO: 3.07 ± 0.36; CHOCHO: 0.03 ± 0.0026) of all species were the least during the typhoon period, indicating that the vertical transport induced by the typhoon significantly increased the height of pollutant distribution, especially for HCHO, which persisted at 1–3 km (Fig. 6g).
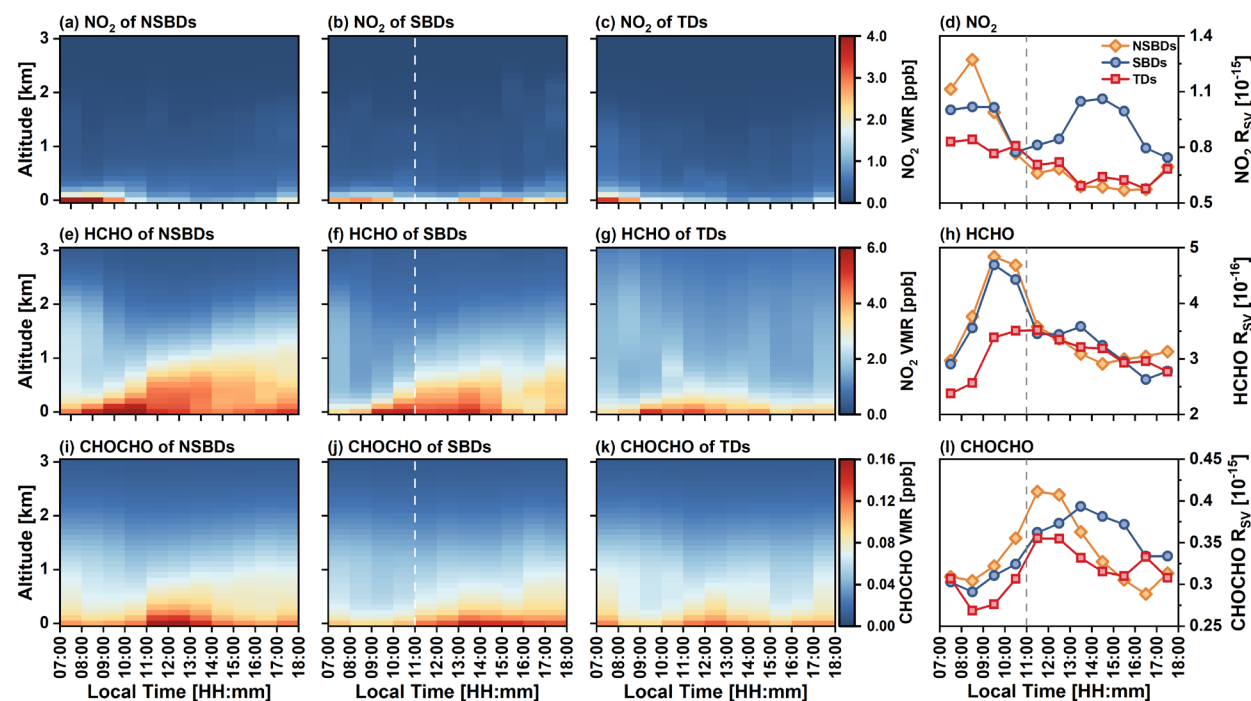
Figure 6. Diurnal variations in vertical distributions of pollutants under different air currents. Mean diurnal vertical distribution of (a–c) NO$_2$, (e–g) HCHO, and (i–k) CHOCHO on NSBDs, SBDs, and TDs. Diurnal variations of the ratios of surface VMRs and VCDs (R_{VS}) for (d) NO$_2$, (h) HCHO and (l) CHOCHO are shown in the far right column. The O$_{time}$ of the SB is indicated in the SBDs and R_{SV} panel by a white dashed line and a grey dotted line, respectively.

3.3 Ozone and photochemical indicators under different air currents

To investigate the influence of different ACPs on summertime O$_3$ concentration and photochemical formation, K-means clustering was to characterize diurnal pattern of O$_3$ concentration (S3 (Supplements)). Figure 7 shows the daily profiles of O$_3$ and its precursors (NO$_2$ and HCHO from MAX-DOAS) and meteorological parameters (temperature, RH and total precipitation (TP)) for the five categories during the observation period. The morning minimum concentration is defined as the background level, while the difference between the midday peak and the morning minimum represents net O$_3$ increment (ΔO$_3$). The statistics on the number of days, background levels, ΔO$_3$, NSBDs and SBDs for each category are shown in Table

S5. Five O_3 clusters exhibit different concentration characteristics: Cluster 1 (moderate background/low ΔO_3), Cluster 2 (low
background/high ΔO_3), Cluster 3 (low background/extreme ΔO_3), Cluster 4 (high background/low ΔO_3), and Cluster 5 (low
background/moderate-high ΔO_3). Moreover, Cluster 1 and Cluster 5 exhibit a high prevalence of SBDs, accounting for 64.7%
and 83.3%, respectively, while Clusters 3 and 4 are predominantly composed of NSBDs, at 71.4% and 86.7%. Cluster 2 shows
an equal distribution of 50% each.

O_3 concentrations are influenced by meteorological factors such as temperature, RH, solar radiation and wind. In general,
strong solar radiation, high surface air temperatures and low RH favor the photochemical production of O_3, leading to increased
O_3 concentrations (Yang et al., 2024). Specifically, in Clusters 1and 5, a higher proportion of SBDs results in lower
temperatures and elevated RH, leading to significantly reduced overall O_3 levels (20.1 ± 3.3 and 15.3 ± 5.3 ppbv). In contrast,
Cluster 3 and 4, dominated by NSBDs, experience higher temperatures and lower RH, which favor O_3 formation, thereby
yielding higher O_3 concentrations (25.4 ± 10.7 and 27.3 ± 3.9 ppbv). Specific daily variations can also be seen, following the
arrival of marine air, the decrease in O_3 concentration in Clusters 1 and 5 is more pronounced than that in Cluster 3 and 4,
occurring nearly in tandem with decreases in temperature and increases in RH, suggesting that the meteorological shifts
induced by the SB are generally unfavorable for O_3 formation (Fig. 7a,b,c). The correlations between ΔO_3 and both change in
temperature (ΔT, defined as the difference between the daytime maximum and the morning minimum) and change in RH
(ΔRH, defined as the difference between the morning maximum and the daytime minimum) further corroborate this conclusion
(Fig. S11). Compared to NSBDs, ΔT exhibited a weaker positive correlation ($R^2 = 0.24$) with ΔO_3 during marine breeze periods
while maintaining a consistent negative correlation ($R^2 = 0.38$) with ΔRH, suggesting that SB arrival suppressed photochemical
O_3 production.

Clusters 1 and 4 exhibit relatively low daytime ΔO_3 because both start from elevated nocturnal O_3 baselines. In Cluster 1,
possible compensation by onshore winds sustained moderate O_3 levels despite heavy nighttime precipitation. Lower nocturnal
RH in Cluster 4 inhibited plant stomatal uptake and diminishes dry deposition efficiency, allowing O_3 to be accumulated
(Kavassalis and Murphy, 2017). In contrast, Cluster 5 shows higher ΔO_3 than Clusters 1 and 4, despite its worse meteorological
conditions, for two synergistic reasons: first, intense precipitation and high RH suppress the nocturnal O_3 baseline, and second,
daytime SB transport delivers greater NO_2 precursor loads, enhancing photochemical O_3 production and amplifying the

daytime peak. Cluster 3 features a sharp afternoon increase in O_3—reaching 44.6 ppbv at 18:00 LT—likely driven by elevated

345   midday HCHO concentrations boosting radical production, combined with a weakening NO_2 titration sink as NO_2 levels fall

toward evening (Fig. 7a,e,f). The contribution of ACPs to pollutant was quantified using the cumulative ratio (R_{SN}) of pollutant

concentrations between SBDs and NSBDs across five clusters (Fig. S12). R_{SN} and cumulative R_{SN} approaching 1 or 5 indicate

equivalent contributions, while values exceeding or falling below these thresholds demonstrate SBDs or NSBDs dominance,

respectively. During 11:00–15:00 LT, O_3 R_{SN} for Clusters 1 and 5 (characterized by low temperature, high humidity and high

350   TP) remained below 1, whereas Clusters 2 and 4 (high temperature, low humidity, very low TP) frequently exceeded 1.

Furthermore, O_3 cumulative R_{SN} gradually rose after the O_{time}, marginally surpassing 5 between 14:00–16:00 LT—

considerably weaker than NO_2. These phenomena suggest that, under favorable meteorological conditions (Clusters 2 and 4),

SB-transported precursors (especially NO_2) bolster O_3 formation, whereas under the typically induced adverse conditions

(Clusters 1 and 5), SB prefers to inhibit O_3 production.
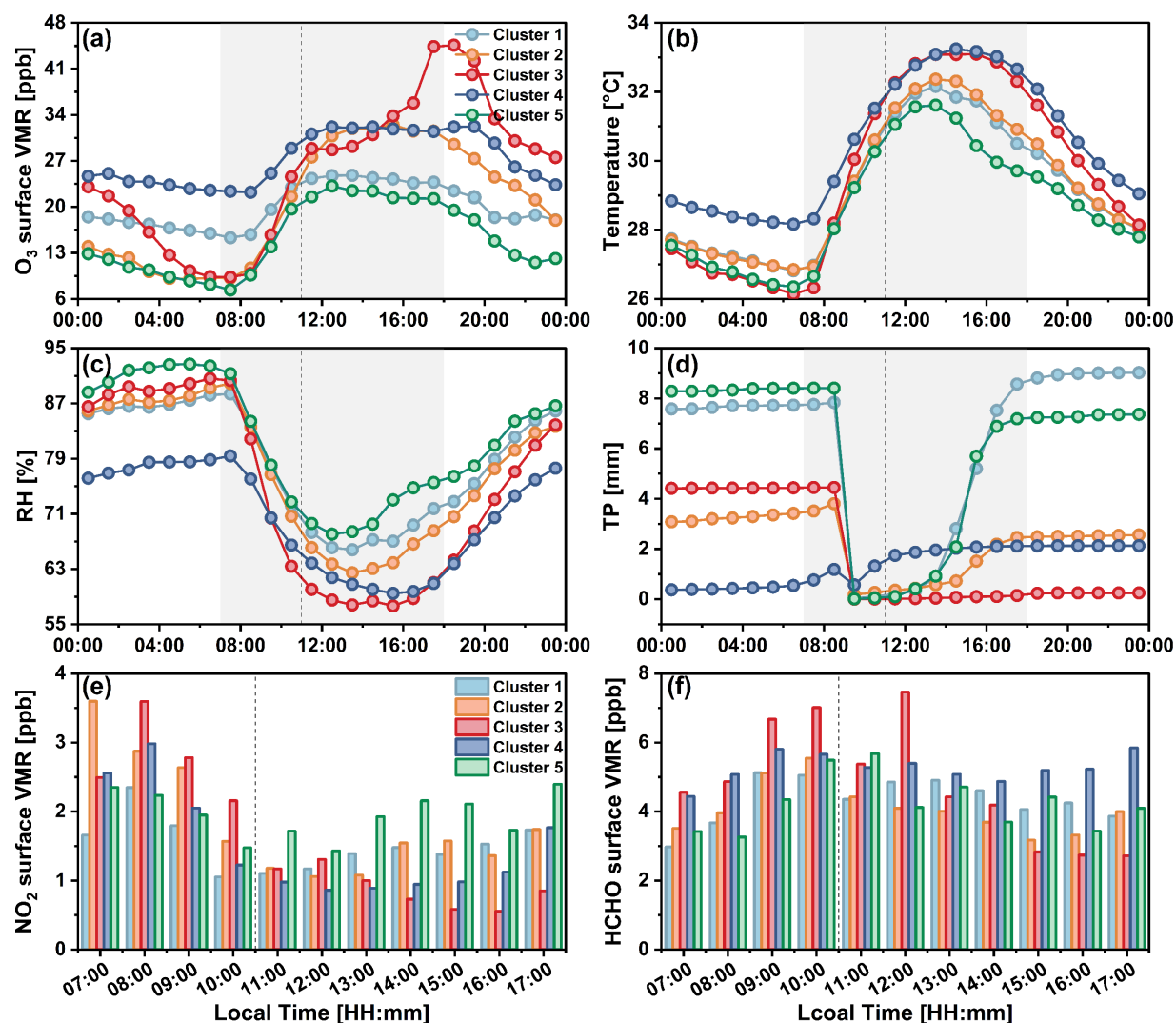
Figure 7. Diurnal variations of O₃, meteorological factors and O₃ precursors in different categories. Mean diurnal cycles of (a) O₃, (b) temperature, (c) RH, (d) total precipitation (TP), (e) NO₂ and (f) HCHO for five categories. MAX-DOAS instrument observation times are indicated by gray shaded areas. The black dotted line indicates when the SB started.

Figure 8 illustrates the diurnal variations in the vertical distributions of R_{GF}, FNR, and GNR under different ACPs, as well as the average characteristics of the vertical profiles. The average surface R_{GF} for three ACPs were 0.024 ± 0.0044, 0.0267 ± 0.0056, and 0.0271 ± 0.0044, all remaining below the 0.04 threshold even during peak daytime concentrations, matching observational records from rural environments (Moortgat et al., 2002; Lee et al., 1995). On NSBDs, enhanced solar radiation

at midday increased CHOCHO concentrations, leading to a simultaneous increase in R_{GF} at the surface (peak 0.03 at 12:00 LT) and in the altitude layer below 300 m. Owing to the distinct vertical distributions of HCHO and CHOCHO, R_{GF} values observed above 300 m decline markedly, and the low-R_{GF} region ($R_{GF} < 0.025$) progressively migrates upward over time (Fig. 6e,i and 8a). The surface R_{GF} exhibits a markedly different pattern on SBDs. Following the onset of the SB, R_{GF} increases steadily until a surface maximum of 0.038 is reached at 16:00, which again proves that the SB transports more VOCs that tend to produce CHOCHO. Aircraft-based photochemical tracer studies indicated that under low-NO_x conditions, isoprene peroxyl radicals (ISOPO2) rapidly isomerize to form CHOCHO (Chan Miller et al., 2017). Given the relatively low local NO_2 levels, it is reasonable to infer that the VOCs introduced by the SB are BVOC (Especially isoprene). The upper R_{GF} also shown a similar upward trend to the near-surface, but is limited to below 300m, suggesting that oceanic air advection transports BVOC mainly in this altitude range (Fig. 8b).

Previous studies have identified regions with biogenic emissions typically showing lower R_{GF} values (< 0.04), while higher R_{GF} (> 0.04) are associated with strong AVOC emissions (Chen et al., 2023; Chan Miller et al., 2014). As shown in Fig. 8d, all ACPs demonstrated mean R_{GF} values < 0.04 across altitudes, indicating BVOC dominance in the FK. On NSBDs, R_{GF} progressively increased with altitude, suggesting higher-altitude VOCs preferentially form CHOCHO over HCHO, consistent with previous findings (Hong et al., 2024; Zhang et al., 2021). The overall higher R_{GF} at 0–2,000 m on SBDs before 10:00 LT may be due to a combination of southerly onshore winds and mountain winds in the morning, which bring the BVOC that has accumulated at high altitude during the night from the mountains to the local area. The 8:00 LT R_{GF} values are high throughout the vertical column, peaking at 700m (0.042), especially below 1,000 m where 54.54% of the R_{GF} exceeds 0.04, suggesting that AVOC may be contributing more here. Due to the transport of BVOC emitted from the vegetation of Wuzhi Mountain by "Prapiroon" to FK, the R_{GF} remained elevated at most heights (especially at the mid-levels) under typhoon conditions, with a peak of 0.038 (at the 800 m). Both SB and typhoon scenarios amplified mid-altitude R_{GF}, demonstrating distinct vertical profiles from NSBDs.
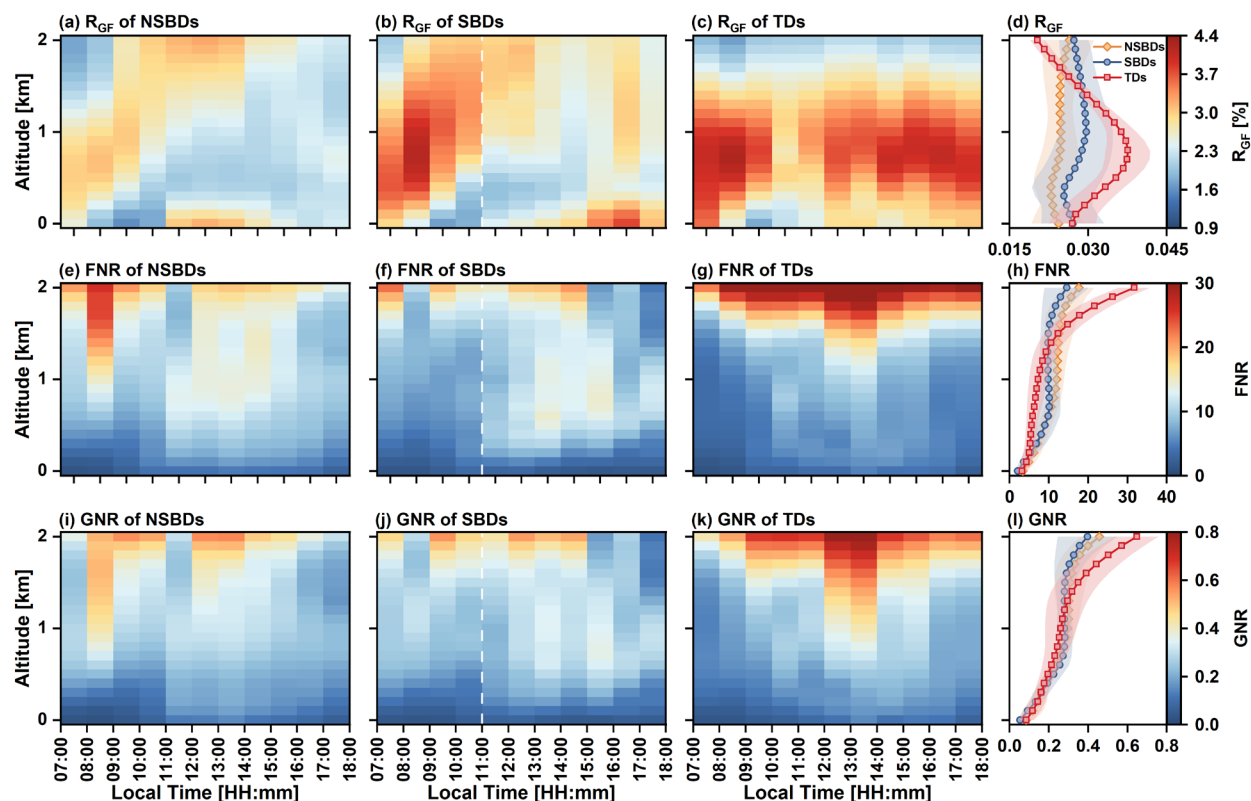
Figure 8. Diurnal variations in vertical distributions of Photochemical indicators. Mean diurnal cycles in the vertical distribution of (a-c) R_{GF}, (e-g) FNR, and (i-k) GNR on NSBDs, SBDs, and TDs. Vertical profiles of (d) R_{GF}, (h) FNR and (l) GNR are shown on the far right, with the shaded area indicating the standard deviation. The O_{time} of the SB is indicated by a white dashed line in the SBDs panel.

Different ACPs have a strong influence on the spatial and temporal distribution of O_3 precursors, especially in SBDs and TDs, where the influx of external precursors can lead to anomalous distributions of pollutant concentrations in the near-surface and upper atmosphere, which may alter the regional O_3 production mechanism (Fig. 6 and 8). The determination of FNR and GNR thresholds is critical for discerning this regime. In this study, a third-order polynomial fit was employed to elucidate the relationship between FNR, GNR, and O_3 concentration (Ren et al., 2022; Jin et al., 2020). Figure 9 shows the strong correlations between O_3 levels and both FNR ($R^2 = 0.94$) and GNR ($R^2 = 0.84$) indicate robust polynomial model performance. We treat the transition state as spanning the first 1% of the indicator range of the O_3 peak, and end up with local near-surface transition zones of FNR and GNR of 6.33–8.90 and 0.16–0.24, respectively. it should be noted that the fitted curves show only

a slight downward trend when the FNR (7.52) and GNR (0.19) are larger than the indicator values with peak O_3 concentrations, and are based on the sparse data, introducing considerable uncertainty. Nevertheless, it is certain that the local thresholds for

400   FNR and GNR are much higher than those reported in previous studies (Liu et al., 2021; Wang et al., 2021). This suggests that the critical importance of localized evaluation for FNR and GNR under conditions of extremely low NO_2 concentrations.
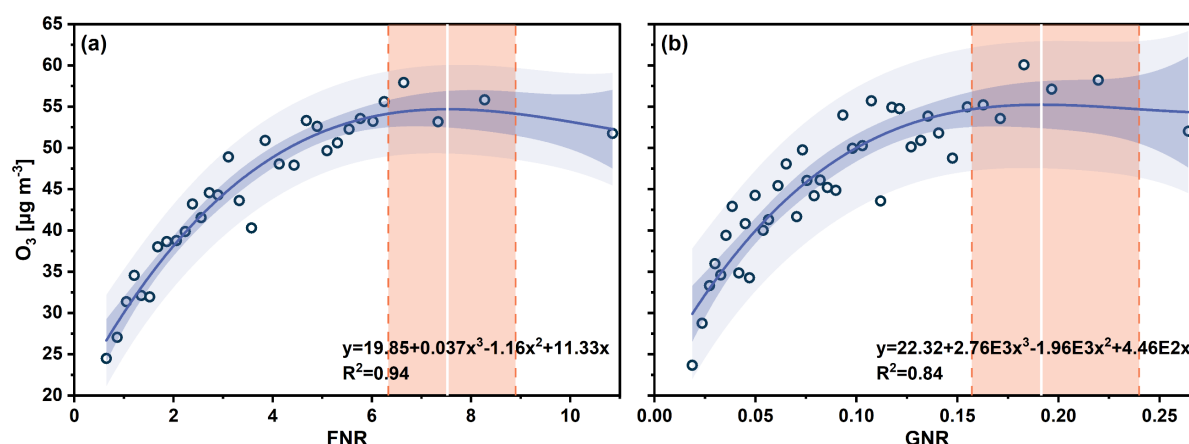
Figure 9. Diagnosing the O_3 formation sensitivity. The relationship between local O_3 surface concentrations and (a) FNR and (b) GNR values was fitted based on MAX-DOAS observations. The blue solid line is the fitted third-order polynomial curve, and the
405   **shading indicates the 95% confidence level and 95% prediction band, respectively. The white solid line indicates the peak of the fitted curve and the pink vertical shading indicates the range above the top 1% of the fitted curve (transition regime).**

Following the OFS thresholds determined, mean surface FNR and GNR for NSBDs (3.92 ± 1.43 and 0.096 ± 0.044), SBDs (2.53 ± 0.82 and 0.065 ± 0.016), and TDs (3.62 ± 1.33 and 0.097 ± 0.037) indicated that the local near-surface was VOC-limited regimes throughout the day. The FNR and GNR under different ACPs revealed pronounced spatiotemporal variations

410   (Fig. 8e–l). On NSBDs and TDs, two indicators follow a synchronized diurnal cycle, rising in the morning to a maximum at 13:00 LT before declining in the afternoon. In contrast, both ratios on SBDs peak synchronously at 12:00 LT (FNR = 3.89, GNR = 0.098), and were then rapidly reduced by the continuously transported NO_2 during the developmental phase of the SB (12:00–15:00 LT), thus strengthening VOC-limited regimes. With the attenuation of SB, reduced external transport and photochemical depletion led to a decline in NO_2 levels, FNR and GNR gradually increase, resulting in a slight shift of the OFS

415   toward the transition regimes, but remained VOC-limited regimes. A mechanism similar to the dual regulation of O_3 production by near-surface SBs still applies at lower atmospheric levels (< 300 m), but it is complicated by the weakening of the NO_2

effect of SB transport with increasing altitude as well as by the heterogeneity of meteorological factors in the vertical direction. The FNR and GNR above 2.5 km on TDs were much higher than those of NSBDs and SBDs throughout the day.

Since the effect of primary emissions on NO_x concentrations decreases with increasing altitude, the sensitivity of O_3 formation to NO_x may increase, leading to an overall increase in FNR and GNR with altitude for all ACPs (Fig. 8h,l). Specifically, less primary emissions and wind dilution on typhoon days resulted in an exponential increase in both metrics with altitude. In particular, above 2.5 km, the FNR and GNR are much larger than those of NSBDs and SBDs throughout the day (Fig. 8g,k). The SB inhibited the vertical transport of pollutants, resulting in a reduced sensitivity of the NO_2 concentration response at high altitude to anthropogenic emissions, so that above 600 m, the FNR is lower on SBDs than on NSBDs, and the difference progressively widens with increasing altitude. This vertical difference feature is weaker in GNR, which is attributed to the fact that CHOCHO is mainly dominated by the oxidation pathway of VOCs rather than the transport process, compared to HCHO. Below 900 m, the photo-oxidation of VOCs and its more significant vertical diffusion advantage over NO_2 together drive the sharp increase in FNR and GNR with altitude. However, from 900 to 1,500 m, both of them show a stabilizing trend, reflecting the synergistic effects of VOCs and NO_x in this altitude range. At higher altitudes, both metrics again showed an increasing trend due to further attenuation of NO_x concentrations.

To further investigate the distribution of OFS across altitudes under different meteorological patterns, we grouped the two metrics below 1.2 km altitude based on local BLH levels and assumed that the same OFS thresholds apply at high altitude and near the ground. Figure 10 shows the contributions of the VOC-limited, transition, and NO_x-limited regimes in each altitude layer on NSBDs, SBDs and TDs. Overall, surface OFS is predominantly VOC-limited regime (contribution >70%), while at higher elevations the VOC contribution decreases and the transitional and NO_x-limited regime become dominant. On SBDs, the contribution of FNR-based transition increases from the 600–800 m layer upward, a trend not seen with the GNR indicator, likely due to differing vertical sensitivities of the two indices to precursors. Below 400 m, the SB inputs more NO_2, resulting in a contribution of more than 50% to the VOC- limited regime in the 0–200 m and 200–400 m layers. Across all meteorological patterns, GNR indicates a high transition regime contribution—over 40% in the 200–400 m and 400–600 m layers. During typhoons, strong turbulence in the boundary layer transports NO_2 upward, thus attenuating the VOC-limited regime at all levels to some extent. With the FNR indicator, all layers except the 1,000–1,200 m layer are VOC-dominated; however, at the GNR

metric, substantial BVOC input results in a predominantly transition and NO$_x$-limited regimes above 200 m. These findings

suggest that (1) GNR may be more suitable as a photochemical indicator of OFS in BVOC-dominated regions than FNR; (2)

reduction of VOC emissions (especially BVOC) can effectively control the local surface O$_3$ pollution; (3) NO$_2$ transport

445   barriers need to be set up below the low elevation in response to the SB, to inhibit the disruption of exogenous pollutants to

photochemical equilibrium of this layer; and (4) The formation process of O$_3$ pollution due to regional and vertical transport

of precursors under extreme weather is more complicated, and needs to be combined with regional joint prevention and control

and vertical pollution control measures.
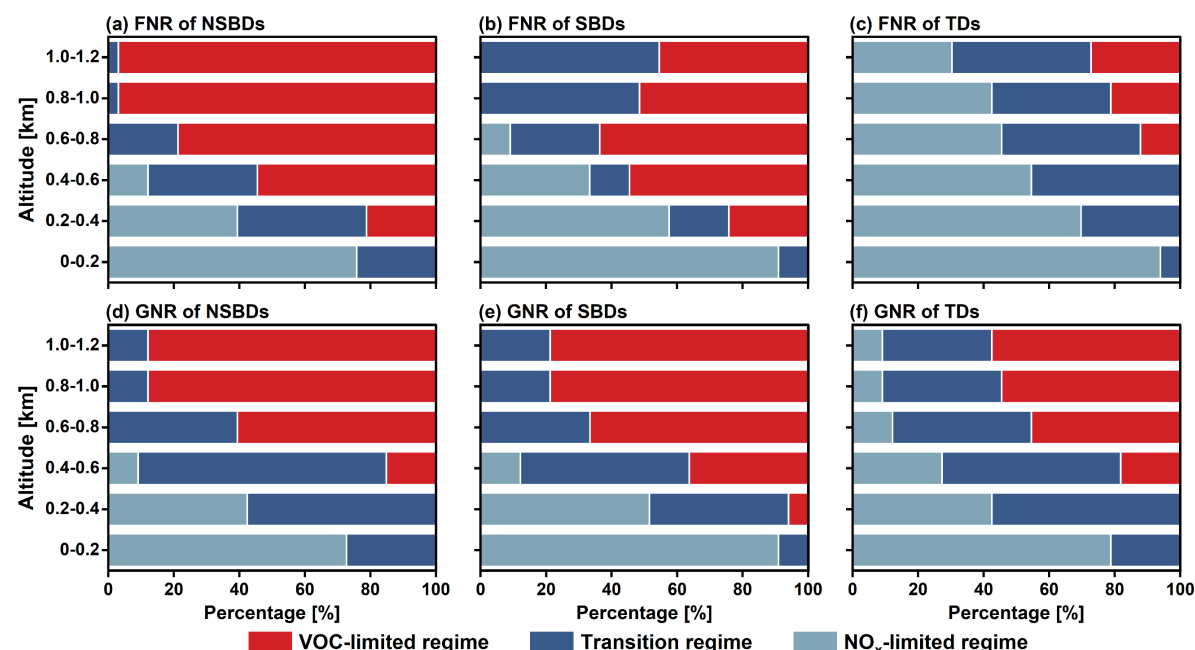
450   **Figure 10. Vertical distributions of ozone formation sensitivity under different air currents. The contribution of VOC-limited, transition, and NO$_x$-limited regimes for each layer below 1.2 km on (a, d) NSBDs, (b, e) SBDs and (c, f) TDs at the observation site.**

4 Discussion

This study employed MAX-DOAS observations to characterize the vertical distribution of daytime aerosols, NO$_2$, HCHO, and

CHOCHO in a coastal rural area of an island environment. The aerosol AOD (0.29 ± 0.1) and NO$_2$ surface VMRs (1.61 ± 0.53

455   ppbv) were substantially lower than those typically observed in urban settings, whereas the HCHO and CHOCHO surface

VMRs (4.33 ± 1.07 and 0.10 ± 0.02 ppbv) were comparable to those in several megacities. HCHO and CHOCHO were closely related to high temperatures and low RH, but due to dilution caused by strong vertical convection, surface HCHO did not show signs of significant elevated midday concentrations similar to those of CHOCHO. The hygroscopic effect of the aerosol caused its vertical distribution pattern to be consistent with the RH. NO_2, HCHO and CHOCHO were concentrated below 300 m, 800 m and 500 m, respectively. Notably, pollutants remaining at higher elevations in the afternoon were transported further upward. The observational findings provide critical insights into the characteristics of pollutants on the NSBDs, SBDs and TDs. In this study, an ORA was established for selecting the first two ACPs. The results demonstrate that the occurrence frequencies of SBDs and NSBDs during local summer reach 33.7% and 34.8%, respectively, with SB typically initiating at 11:00 LT and dissipating by 18:00 LT. Indeed, The ORA can be broadly applied, as parameter tuning and threshold adjustment allow for the selection of circulation patterns that correspond to local characteristics. Nevertheless, precise delineation of NSBDs remains challenging in complex island environments under monsoon influence, as transient cloud cover may introduce anomalies in RH variation indices even on valid NSBDs. Combining the ORA with MAX-DOAS observations, we analyzed the spatial and temporal distributions of pollutants and photochemical indicators (R_{GF}, FNR and GNR) under different ACPs. The overall low R_{GF} values (< 0.04) for all ACPs indicated predominant local BVOC contributions. Elevated concentrations (e.g., O_3) and vertical distribution (e.g., HCHO, CHOCHO) of pollutants are observed on NSBDs, driven by highly favorable meteorological conditions that enhance VOCs photochemical oxidation and vertical dispersion, necessitating stringent controls on precursor emissions and transport process under this pattern. SB introduced moist air masses that cooled surface temperatures and its vertical structure reduced BLH, suppressing pollutant generation and dispersion. Notably, SB intrusion enhanced NO_2 and BVOC transport below 300 m, which may enhance O_3 production under suitable conditions. Typhoons minimized pollutant concentrations through strong dilution by wind and precipitation, yet simultaneously elevated mid-altitude BVOC via regional transport and promoted vertical dispersion through intense turbulence.

Vertical heterogeneity in OFS under distinct ACPs reveals complex dependence of O_3 formation on airflow-driven precursors. Local surface O_3 formation showed VOC-sensitive characteristics based on FNR and GNR, transitioning to NO_x-limited regime with altitude, but VOC-limited regime still contributed to OFS at high altitude on TDs. Additional BVOC inputs from SB and typhoons and strong local biological discharges suggest that GNR may be a more appropriate indicator of OFS. It

should be noted that our determined FNR and GNR thresholds significantly exceeded literature values, suggesting existing classification criteria may inadequately represent tropical coastal rural environments with low NO_2 baseline concentrations. Overall, abatement of VOCs is an effective means to manage local O_3, while the basic strategy of controlling the emission of NO_x as well as VOCs from the SB may help to reduce local photochemical pollution. It should be noted that we cannot accurately determine the OFS in the vertical direction because the DPS only provides surface O_3 concentration data and carry over the surface OFS thresholds to other altitudes introduces a large uncertainty. Future work should aim to develop local FNR and GNR thresholds in the vertical direction for more accurate assessments.

Data available. The MAX-DOAS datasets generated in this study are available from the corresponding authors (S.W.) upon reasonable request for research purposes. O_3 data can be downloaded from the https://www.mee.gov.cn, ERA5 pressure-level data can be downloaded from https://cds.climate.copernicus.eu/datasets/reanalysis-era5-pressure-levels?tab=overview, ERA5 single-level data can be downloaded from https://cds.climate.copernicus.eu/datasets/reanalysis-era5-single-levels?tab=overview, ERA5-Land data can be downloaded from https://cds.climate.copernicus.eu/datasets/reanalysis-era5-land?tab=overview.

Author Contributions. B. L., S. Z., and Z. J. set up and operated the MAX-DOAS instrument, and B. L. analyzed the data with the help of S. Z., Y. S., and Z. J.; B. L. wrote the manuscript, S. W., B. Z., S. Z., and R. X. provided comments, and S. W. conceived, supervised, reviewed and edited the paper. All authors participated in the discussion of the results and revision of the manuscript.

Competing interests. The authors declare that they have no competing interests.

Acknowledgements. This study has been supported by National Natural Science Foundation of China (42375089, W2411028), National Key Research and Development Program of China (2023YFC3709401 and 2023YFC3709400), and National Civilian Space Infrastructure Project (Grant No. Y5BZ31AC60). The authors would like to thank the Chinese Ministry of Ecology and

Environment for providing the O_3 data and to the developers of the ERA5 data for providing free and Open-access materials. The authors would like to thank the Institute of Remote Sensing/Institute of Environmental Physics, University of Bremen, Germany, for providing the SCIATRAN radiative transfer model used in this paper.

510   **Financial support.** This study has been supported by National Natural Science Foundation of China (42375089, W2411028), National Key Research and Development Program of China (2023YFC3709401 and 2023YFC3709400), and National Civilian Space Infrastructure Project (Grant No. Y5BZ31AC60).

References

Arrillaga, J. A., Jiménez, P., Vilà-Guerau de Arellano, J., Jiménez, M. A., Román-Cascón, C., Sastre, M., and Yagüe, C.:

515   Analyzing the Synoptic-, Meso- and Local- Scale Involved in Sea Breeze Formation and Frontal Characteristics, J. Geophys. Res.: Atmos., 125, https://doi.org/10.1029/2019jd031302, 2020.

Arrillaga, J. A., Yagüe, C., Sastre, M., and Román-Cascón, C.: A characterisation of sea-breeze events in the eastern Cantabrian coast (Spain) from observational data and WRF simulations, Atmos. Res., 181, 265-280, https://doi.org/10.1016/j.atmosres.2016.06.021, 2016.

520   Azorin-Molina, C., Connell, B. H., and Baena-Calatrava, R.: Sea-Breeze Convergence Zones from AVHRR over the Iberian Mediterranean Area and the Isle of Mallorca, Spain, J. Appl. Meteorol. Climatol., 48, 2069-2085, https://doi.org/10.1175/2009JAMC2141.1, 2009.

Azorin-Molina, C., Tijm, S., and Chen, D.: Development of selection algorithms and databases for sea breeze studies, Theor. Appl. Climatol., 106, 531-546, https://doi.org/10.1007/s00704-011-0454-4, 2011.

525   Barthlott, C. and Kirshbaum, D. J.: Sensitivity of deep convection to terrain forcing over Mediterranean islands, Q. J. R. Meteorolog. Soc., 139, 1762-1779, https://doi.org/10.1002/qj.2089, 2013.

Benish, S. E., He, H., Ren, X., Roberts, S. J., Salawitch, R. J., Li, Z., Wang, F., Wang, Y., Zhang, F., Shao, M., Lu, S., and Dickerson, R. R.: Measurement report: Aircraft observations of ozone, nitrogen oxides, and volatile organic compounds over Hebei Province, China, Atmos. Chem. Phys., 20, 14523-14545, https://doi.org/10.5194/acp-20-14523-2020, 2020.

530 Chan Miller, C., Gonzalez Abad, G., Wang, H., Liu, X., Kurosu, T., Jacob, D. J., and Chance, K.: Glyoxal retrieval from the Ozone Monitoring Instrument, Atmos. Meas. Tech., 7, 3891-3907, https://doi.org/10.5194/amt-7-3891-2014, 2014.

Chan Miller, C., Jacob, D. J., Marais, E. A., Yu, K., Travis, K. R., Kim, P. S., Fisher, J. A., Zhu, L., Wolfe, G. M., Hanisco, T. F., Keutsch, F. N., Kaiser, J., Min, K. E., Brown, S. S., Washenfelder, R. A., González Abad, G., and Chance, K.: Glyoxal yield from isoprene oxidation and relation to formaldehyde: chemical mechanism, constraints from SENEX aircraft
535 observations, and interpretation of OMI satellite data, Atmos. Chem. Phys., 17, 8725-8738, https://doi.org/10.5194/acp-17-8725-2017, 2017.

Chang, B., Liu, H., Zhang, C., Xing, C., Tan, W., and Liu, C.: Relating satellite NO_2 tropospheric columns to near-surface concentrations: implications from ground-based MAX-DOAS NO_2 vertical profile observations, npj Clim. Atmos. Sci., 8, https://doi.org/10.1038/s41612-024-00891-z, 2025.

540 Chauhan, B. V. S., Smallbone, K. L., Berg, M., and Wyche, K. P.: The temporal evolution of HCHO and changes in atmospheric composition in the southeast of the United Kingdom, Case Stud. Chem. Environ. Eng., 11, 101092, https://doi.org/10.1016/j.cscee.2024.101092, 2025.

Chen, Y., Liu, C., Su, W., Hu, Q., Zhang, C., Liu, H., and Yin, H.: Identification of volatile organic compound emissions from anthropogenic and biogenic sources based on satellite observation of formaldehyde and glyoxal, Sci. Total Environ., 859,
545 159997, https://doi.org/10.1016/j.scitotenv.2022.159997, 2023.

Cheng, T., Xu, C., Duan, J., Wang, Y., Leng, C., Tao, J., Che, H., He, Q., Wu, Y., Zhang, R., Li, X., Chen, J., Kong, L., and Yu, X.: Seasonal variation and difference of aerosol optical properties in columnar and surface atmospheres over Shanghai, Atmos. Environ., 123, 315-326, https://doi.org/10.1016/j.atmosenv.2015.05.029, 2015.

Cooke, M. C., Utembe, S. R., Carbajo, P. G., Archibald, A. T., Orr-Ewing, A. J., Jenkin, M. E., Derwent, R. G., Lary, D. J., and
550 Shallcross, D. E.: Impacts of formaldehyde photolysis rates on tropospheric chemistry, Atmos. Sci. Lett., 11, 33-38, https://doi.org/10.1002/asl.251, 2010.

Cuxart, J., Jiménez, M. A., Telišman Prtenjak, M., and Grisogono, B.: Study of a Sea-Breeze Case through Momentum, Temperature, and Turbulence Budgets, J. Appl. Meteorol. Climatol., 53, 2589-2609, https://doi.org/10.1175/jamc-d-14-0007.1, 2014.

555   Deng, T., Wang, T., Wang, S., Zou, Y., Yin, C., Li, F., Liu, L., Wang, N., Song, L., Wu, C., and Wu, D.: Impact of typhoon periphery on high ozone and high aerosol pollution in the Pearl River Delta region, Sci. Total Environ., 668, 617-630, https://doi.org/10.1016/j.scitotenv.2019.02.450, 2019.

Duncan, B. N., Yoshida, Y., Olson, J. R., Sillman, S., Martin, R. V., Lamsal, L., Hu, Y., Pickering, K. E., Retscher, C., Allen, D. J., and Crawford, J. H.: Application of OMI observations to a space-based indicator of NO_x and VOC controls on

560   surface ozone formation, Atmos. Environ., 44, 2213-2223, https://doi.org/10.1016/j.atmosenv.2010.03.010, 2010.

Franco, B., Hendrick, F., Van Roozendael, M., Mueller, J. F., Stavrakou, T., Marais, E. A., Bovy, B., Bader, W., Fayt, C., Hermans, C., Lejeune, B., Pinardi, G., Servais, C., and Mahieu, E.: Retrievals of formaldehyde from ground-based FTIR and MAX-DOAS observations at the Jungfraujoch station and comparisons with GEOS-Chem and IMAGES model simulations, Atmos. Meas. Tech., 8, 1733-1756, https://doi.org/10.5194/amt-8-1733-2015, 2015.

565   Frieß, U., Monks, P. S., Remedios, J. J., Rozanov, A., Sinreich, R., Wagner, T., and Platt, U.: MAX-DOAS O_4 measurements: A new technique to derive information on atmospheric aerosols: 2. Modeling studies, J. Geophys. Res.: Atmos., 111, https://doi.org/10.1029/2005JD006618, 2006.

Frieß, U., Sihler, H., Sander, R., Pöhler, D., Yilmaz, S., and Platt, U.: The vertical distribution of BrO and aerosols in the Arctic: Measurements by active and passive differential optical absorption spectroscopy, J. Geophys. Res.: Atmos., 116,

570   https://doi.org/10.1029/2011JD015938, 2011.

Fu, C., Dan, L., Tong, J., and Xu, W.: Influence of Typhoon Nangka Process on Ozone Pollution in Hainan Island, Huanjing Kexue, 44, 2481-2491, https://doi.org/10.13227/j.hjkx.202206123, 2023.

Fu, G., Yu, J., Zhang, Y., Hu, S., Ouyang, R., and Liu, W.: Temporal variation of wind speed in China for 1961-2007, Theor. Appl. Climatol., 104, 313-324, https://doi.org/10.1007/s00704-010-0348-x, 2011.

575   Gangoiti, G., Alonso, L., Navazo, M., Albizuri, A., Perez-Landa, G., Matabuena, M., Valdenebro, V., Maruri, M., Antonio García, J., and Millán, M. M.: Regional transport of pollutants over the Bay of Biscay: analysis of an ozone episode under a blocking anticyclone in west-central Europe, Atmos. Environ., 36, 1349-1361, https://doi.org/10.1016/S1352-2310(01)00536-2, 2002.

Glaser, K., Vogt, U., Baumbach, G., Volz-Thomas, A., and Geiss, H.: Vertical profiles of O_3, NO_2, NO_x, VOC, and

580   meteorological parameters during the Berlin Ozone Experiment (BERLIOZ) campaign, Journal of Geophysical Research-

Atmospheres, 108, https://doi.org/10.1029/2002jd002475, 2003.

Gordon, G. E.: Atmospheric science: atmospheric chemistry and atmospheric chemistry and physics of air pollution, Science

(New York, N.Y.), 235, 1263b-1264b, https://doi.org/10.1126/science.235.4793.1263b, 1987.

Guo, H., Xu, M., and Hu, Q.: Changes in near-surface wind speed in China: 1969-2005, Int. J. Climatol., 31, 349-358,

585   https://doi.org/10.1002/joc.2091, 2011.

Hendrick, F., Müller, J. F., Clémer, K., Wang, P., De Mazière, M., Fayt, C., Gielen, C., Hermans, C., Ma, J. Z., Pinardi, G.,

Stavrakou, T., Vlemmix, T., and Van Roozendael, M.: Four years of ground-based MAX-DOAS observations of HONO

and NO_2 in the Beijing area, Atmos. Chem. Phys., 14, 765-781, https://doi.org/10.5194/acp-14-765-2014, 2014.

Henyey, L. G. and Greenstein, J. L.: Diffuse radiation in the galaxy, Astrophys. J., 93, 70-83, https://doi.org/10.1086/144246,

590   1941.

Hong, Q., Liu, C., Hu, Q., Zhang, Y., Xing, C., Ou, J., Tan, W., Liu, H., Huang, X., and Wu, Z.: Vertical distribution and

temporal evolution of formaldehyde and glyoxal derived from MAX-DOAS observations: The indicative role of VOC

sources, J Environ Sci (China), 122, 92-104, https://doi.org/10.1016/j.jes.2021.09.025, 2022.

Hong, Q., Xing, J., Xing, C., Yang, B., Su, W., Chen, Y., Zhang, C., Zhu, Y., and Liu, C.: Investigating vertical distributions

595   and photochemical indications of formaldehyde, glyoxal, and NO_2 from MAX-DOAS observations in four typical cities

of China, Sci. Total Environ., 954, https://doi.org/10.1016/j.scitotenv.2024.176447, 2024.

Jiang, F., Wang, T., Wang, T., Xie, M., and Zhao, H.: Numerical modeling of a continuous photochemical pollution episode in

Hong Kong using WRF–chem, Atmos. Environ., 42, 8717-8727, https://doi.org/10.1016/j.atmosenv.2008.08.034, 2008.

Jiang, Z., Wang, S., Yan, Y., Zhang, S., Xue, R., Gu, C., Zhu, J., Liu, J., and Zhou, B.: Constructing the 3D Spatial Distribution

600   of the $HCHO/NO_2$ Ratio via Satellite Observation and Machine Learning Model, Environ. Sci. Technol., 59, 4047-4058,

https://doi.org/10.1021/acs.est.4c12362, 2025.

Jin, X., Fiore, A., Boersma, K. F., Smedt, I. D., and Valin, L.: Inferring Changes in Summertime Surface Ozone–NO_x–VOC

Chemistry over U.S. Urban Areas from Two Decades of Satellite and Ground-Based Observations, Environ. Sci. Technol.,

54, 6518-6529, https://doi.org/10.1021/acs.est.9b07785, 2020.

605 Kavassalis, S. C. and Murphy, J. G.: Understanding ozone-meteorology correlations: A role for dry deposition, Geophys. Res. Lett., 44, 2922-2931, https://doi.org/10.1002/2016gl071791, 2017.

KiranKumar, N. V. P., Jagadeesh, K., Niranjan, K., and Rajeev, K.: Seasonal variations of sea breeze and its effect on the spectral behaviour of surface layer winds in the coastal zone near Visakhapatnam, India, J. Atmos. Sol. Terr. Phys., 186, 1-7, https://doi.org/10.1016/j.jastp.2019.01.013, 2019.

610 Kumar, V., Beirle, S., Dörner, S., Mishra, A. K., Donner, S., Wang, Y., Sinha, V., and Wagner, T.: Long-term MAX-DOAS measurements of NO_2, HCHO, and aerosols and evaluation of corresponding satellite data products over Mohali in the Indo-Gangetic Plain, Atmos. Chem. Phys., 20, 14183-14235, https://doi.org/10.5194/acp-20-14183-2020, 2020.

Lee, Y.-N., Zhou, X., and Hallock, K.: Atmospheric carbonyl compounds at a rural southeastern United States site, J. Geophys. Res.: Atmos., 100, 25933-25944, https://doi.org/10.1029/95JD02605, 1995.

615 Li, H., Gong, W., Liu, B., Ma, Y., Jin, S., Wang, W., Fan, R., Jiang, S., Wang, Y., and Tong, Z.: Sea Breeze-Driven Variations in Planetary Boundary Layer Height over Barrow: Insights from Meteorological and Lidar Observations, Remote Sens., 17, 1633, https://www.mdpi.com/2072-4292/17/9/1633, 2025.

Li, Z., Song, L., Ma, H., Xiao, J., Wang, K., and Chen, L.: Observed surface wind speed declining induced by urbanization in East China, Clim. Dyn., 50, 735-749, https://doi.org/10.1007/s00382-017-3637-6, 2018.

620 Liang, Z. and Wang, D.: Sea breeze and precipitation over Hainan Island, Q. J. R. Meteorolog. Soc., 143, 137-151, https://doi.org/10.1002/qj.2952, 2017.

Liu, G. and Wang, Y.: Vertical distribution characteristics and potential sources of atmospheric pollutants in the North China Plain basing on the MAX-DOAS measurement, Environ. Sci. Eur., 36, 78, https://doi.org/10.1186/s12302-024-00902-z, 2024.

625 Liu, J., Li, X., Tan, Z., Wang, W., Yang, Y., Zhu, Y., Yang, S., Song, M., Chen, S., Wang, H., Lu, K., Zeng, L., and Zhang, Y.: Assessing the Ratios of Formaldehyde and Glyoxal to NO_2 as Indicators of O_3–NO_x–VOC Sensitivity, Environ. Sci. Technol., 55, 10935-10945, https://doi.org/10.1021/acs.est.0c07506, 2021.

Liu, Q., Liu, D., Gao, Q., Tian, P., Wang, F., Zhao, D., Bi, K., Wu, Y., Ding, S., Hu, K., Zhang, J., Ding, D., and Zhao, C.: Vertical characteristics of aerosol hygroscopicity and impacts on optical properties over the North China Plain during

630   winter, Atmos. Chem. Phys., 20, 3931-3944, https://doi.org/10.5194/acp-20-3931-2020, 2020.

Liu, S., Cheng, S., Ma, J., Xu, X., Lv, J., Jin, J., Guo, J., Yu, D., and Dai, X.: MAX-DOAS Measurements of Tropospheric NO_2 and HCHO Vertical Profiles at the Longfengshan Regional Background Station in Northeastern China, Sensors, 23, https://doi.org/10.3390/s23063269, 2023.

Lou, Y., Chen, Y., Chen, X., and Li, R.: Spatiotemporal estimates of anthropogenic NO_x emissions across China during 2015-

635   2022 using a deep learning model, J. Hazard. Mater., 487, https://doi.org/10.1016/j.jhazmat.2025.137308, 2025.

Martins, D. K., Stauffer, R. M., Thompson, A. M., Knepp, T. N., and Pippin, M.: Surface ozone at a coastal suburban site in 2009 and 2010: Relationships to chemical and meteorological processes, J. Geophys. Res.: Atmos., 117, https://doi.org/10.1029/2011JD016828, 2012.

Mason, R. S.: Atmospheric Photochemistry, in: Applied Photochemistry, edited by: Evans, R. C., Douglas, P., and Burrow, H.

640   D., Springer Netherlands, Dordrecht, 217-246, 10.1007/978-90-481-3830-2_5, 2013.

Miller, S. T. K., Keim, B. D., Talbot, R. W., and Mao, H.: Sea breeze: Structure, forecasting, and impacts, Rev. Geophys., 41, https://doi.org/10.1029/2003rg000124, 2003.

Moortgat, G. K., Grossmann, D., Boddenberg, A., Dallmann, G., Ligon, A. P., Turner, W. V., Gäb, S., Slemr, F., Wieprecht, W., Acker, K., Kibler, M., Schlomski, S., and Bächmann, K.: Hydrogen Peroxide, Organic Peroxides and Higher Carbonyl

645   Compounds Determined during the BERLIOZ Campaign, J. Atmos. Chem., 42, 443-463, https://doi.org/10.1023/A:1015743013107, 2002.

Parker, D. J.: MESOSCALE METEOROLOGY | Overview, in: Encyclopedia of Atmospheric Sciences (Second Edition), edited by: North, G. R., Pyle, J., and Zhang, F., Academic Press, Oxford, 316-322, 10.1016/B978-0-12-382225-3.00478-3, 2015.

650   Puygrenier, V., Lohou, F., Campistron, B., Saïd, F., Pigeon, G., Bénech, B., and Serça, D.: Investigation on the fine structure of sea-breeze during ESCOMPTE experiment, Atmos. Res., 74, 329-353, https://doi.org/10.1016/j.atmosres.2004.06.011, 2005.

Qu, K., Wang, X., Yan, Y., Shen, J., Xiao, T., Dong, H., Zeng, L., and Zhang, Y.: A comparative study to reveal the influence of typhoons on the transport, production and accumulation of O_3 in the Pearl River Delta, China, Atmos. Chem. Phys.,

655   21, 11593-11612, https://doi.org/10.5194/acp-21-11593-2021, 2021.

Ren, J., Guo, F., and Xie, S.: Diagnosing ozone–NO$_x$–VOC sensitivity and revealing causes of ozone increases in China based on 2013–2021 satellite retrievals, Atmos. Chem. Phys., 22, 15035-15047, https://doi.org/10.5194/acp-22-15035-2022, 2022.

Roux, F., Clark, H., Wang, K. Y., Rohs, S., Sauvage, B., and Nédélec, P.: The influence of typhoons on atmospheric composition
660   deduced from IAGOS measurements over Taipei, Atmos. Chem. Phys., 20, 3945-3963, https://doi.org/10.5194/acp-20-3945-2020, 2020.

Rozanov, V. V., Buchwitz, M., Eichmann, K. U., de Beek, R., and Burrows, J. P.: Sciatran - a new radiative transfer model for geophysical applications in the 240–2400 NM spectral region: the pseudo-spherical version, Adv. Space Res., 29, 1831-1835, https://doi.org/10.1016/S0273-1177(02)00095-9, 2002.

665   Song, X., Li, X.-B., Yuan, B., He, X., Chen, Y., Wang, S., Huangfu, Y., Peng, Y., Zhang, C., Liu, A., Yang, H., Liu, C., Li, J., and Shao, M.: Elucidating key factors in regulating budgets of ozone and its precursors in atmospheric boundary layer, npj Clim. Atmos. Sci., 7, https://doi.org/10.1038/s41612-024-00818-8, 2024.

Talbot, C., Augustin, P., Leroy, C., Willart, V., Delbarre, H., and Khomenko, G.: Impact of a sea breeze on the boundary-layer dynamics and the atmospheric stratification in a coastal area of the North Sea, Boundary Layer Meteorol., 125, 133-154,
670   https://doi.org/10.1007/s10546-007-9185-6, 2007.

Vo, T.-D.-H., Lin, C., Weng, C.-E., Yuan, C. S., Lee, C.-W., Hung, C.-H., Xuan-Thanh, B., Lo, K.-C., and Lin, J.-X.: Vertical stratification of volatile organic compounds and their photochemical product formation potential in an industrial urban area, J. Environ. Manage., 217, 327-336, https://doi.org/10.1016/j.jenvman.2018.03.101, 2018.

Vrekoussis, M., Wittrock, F., Richter, A., and Burrows, J. P.: GOME-2 observations of oxygenated VOCs: what can we learn
675   from the ratio glyoxal to formaldehyde on a global scale?, Atmos. Chem. Phys., 10, 10145-10160, https://doi.org/10.5194/acp-10-10145-2010, 2010.

Wagner, T., Beirle, S., Brauers, T., Deutschmann, T., Friess, U., Hak, C., Halla, J. D., Heue, K. P., Junkermann, W., Li, X., Platt, U., and Pundt-Gruber, I.: Inversion of tropospheric profiles of aerosol extinction and HCHO and NO$_2$ mixing ratios from MAX-DOAS observations in Milano during the summer of 2003 and comparison with independent data sets, Atmos.

680   Meas. Tech., 4, 2685-2715, https://doi.org/10.5194/amt-4-2685-2011, 2011.

Wang, J., Wang, P., Tian, C., Gao, M., Cheng, T., and Mei, W.: Consecutive Northward Super Typhoons Induced Extreme Ozone Pollution Events in Eastern China, npj Clim. Atmos. Sci., 7, https://doi.org/10.1038/s41612-024-00786-z, 2024.

Wang, W., van der A, R., Ding, J., van Weele, M., and Cheng, T.: Spatial and temporal changes of the ozone sensitivity in China based on satellite and ground-based observations, Atmos. Chem. Phys., 21, 7253-7269, https://doi.org/10.5194/acp-21-7253-2021, 2021.

685

Wang, Z., Zhang, H., Shi, C., Ji, X., Zhu, Y., Xia, C., Sun, X., Zhang, M., Lin, X., Yan, S., Zhou, Y., Xing, C., Chen, Y., and Liu, C.: Vertical and spatial differences in ozone formation sensitivities under different ozone pollution levels in eastern Chinese cities, npj Clim. Atmos. Sci., 8, https://doi.org/10.1038/s41612-024-00855-3, 2025.

Wittrock, F., Richter, A., Oetjen, H., Burrows, J. P., Kanakidou, M., Myriokefalitakis, S., Volkamer, R., Beirle, S., Platt, U., and Wagner, T.: Simultaneous global observations of glyoxal and formaldehyde from space, Geophys. Res. Lett., 33, https://doi.org/10.1029/2006gl026310, 2006.

690

Wu, M., Wu, D., Fan, Q., Wang, B. M., Li, H. W., and Fan, S. J.: Observational studies of the meteorological characteristics associated with poor air quality over the Pearl River Delta in China, Atmos. Chem. Phys., 13, 10755-10766, https://doi.org/10.5194/acp-13-10755-2013, 2013.

695 Xin, J., Ma, Y., Zhao, D., Gong, C., Ren, X., Tang, G., Xia, X., Wang, Z., Cao, J., de Arellano, J. V.-G., and Martin, S. T.: The feedback effects of aerosols from different sources on the urban boundary layer in Beijing China, Environ. Pollut., 325, 121440, https://doi.org/10.1016/j.envpol.2023.121440, 2023.

Xing, C., Liu, C., Hu, Q., Fu, Q., Lin, H., Wang, S., Su, W., Wang, W., Javed, Z., and Liu, J.: Identifying the wintertime sources of volatile organic compounds (VOCs) from MAX-DOAS measured formaldehyde and glyoxal in Chongqing, southwest

700   China, Sci. Total Environ., 715, 136258, https://doi.org/10.1016/j.scitotenv.2019.136258, 2020.

Xu, J., Huang, X., Wang, N., Li, Y., and Ding, A.: Understanding ozone pollution in the Yangtze River Delta of eastern China from the perspective of diurnal cycles, Sci. Total Environ., 752, 141928, https://doi.org/10.1016/j.scitotenv.2020.141928, 2021.

Xu, W., Xing, Q., Pan, L., Wang, Z., Cao, X., Yan, W., Xie, W., Meng, X., and Wu, X.: Characterization, source apportionment,

705  and risk assessment of ambient volatile organic compounds in urban and background regions of Hainan Island, China, Atmos. Environ., 316, 120167, https://doi.org/10.1016/j.atmosenv.2023.120167, 2024.

Yan, H. and Anthes, R. A.: THE EFFECT OF VARIATIONS IN SURFACE MOISTURE ON MESOSCALE CIRCULATIONS, Mon. Weather Rev., 116, 192-208, https://doi.org/10.1175/1520-0493(1988)116, 1988.

Yang, J. X., Lau, A. K. H., Fung, J. C. H., Zhou, W., and Wenig, M.: An air pollution episode and its formation mechanism

710  during the tropical cyclone Nuri's landfall in a coastal city of south China, Atmos. Environ., 54, 746-753, https://doi.org/10.1016/j.atmosenv.2011.12.023, 2012.

Yang, Y., Zhou, Y., Wang, H., Li, M., Li, H., Wang, P., Yue, X., Li, K., Zhu, J., and Liao, H.: Meteorological characteristics of extreme ozone pollution events in China and their future predictions, Atmos. Chem. Phys., 24, 1177-1191, https://doi.org/10.5194/acp-24-1177-2024, 2024.

715 Yu, Y., Zhou, H., Zhao, Z., Chang, Y., Wu, D., Li, Z., Wang, F., Fang, M., and Zhou, X.: Spatiotemporal Distribution, Meteorological Influence, and Potential Sources of Air Pollution over Hainan Island, China, Atmosphere, 15, 1336, https://www.mdpi.com/2073-4433/15/11/1336, 2024.

Zhan, J., Zheng, F., Xie, R., Liu, J., Chu, B., Ma, J., Xie, D., Meng, X., Huang, Q., He, H., and Liu, Y.: The role of NO_x in Co-occurrence of O_3 and $PM_{2.5}$ pollution driven by wintertime east Asian monsoon in Hainan, J. Environ. Manage., 345,

720  118645, https://doi.org/10.1016/j.jenvman.2023.118645, 2023.

Zhang, S., Wang, S., Zhang, R., Guo, Y., Yan, Y., Ding, Z., and Zhou, B.: Investigating the Sources of Formaldehyde and Corresponding Photochemical Indications at a Suburb Site in Shanghai From MAX-DOAS Measurements, J. Geophys. Res.: Atmos., 126, https://doi.org/10.1029/2020jd033351, 2021.

Zhang, Y., Man, X., Zhang, S., Liu, L., Kong, F., Feng, T., and Liu, R.: Ground-based MAX-DOAS observations of

725  formaldehyde and glyoxal in Xishuangbanna, China, J. Environ. Sci., 152, 328-339, https://doi.org/10.1016/j.jes.2024.04.036, 2025.

Zhang, Z.-z., Cao, C.-x., Song, Y., Kang, L., and Cai, X.-h.: STATISTICAL CHARACTERISTICS AND NUMERICAL SIMULATION OF SEA-LAND BREEZES IN HAINAN ISLAND, J. Trop. Meteorol., 20, 267-278, https://jtm.itmm.org.cn/en/article/id/20140309, 2014.

730   Zhao, D., Xin, J., Wang, W., Jia, D., Wang, Z., Xiao, H., Liu, C., Zhou, J., Tong, L., Ma, Y., Wen, T., Wu, F., and Wang, L.:
        Effects of the sea-land breeze on coastal ozone pollution in the Yangtze River Delta, China, Sci. Total Environ., 807,
        https://doi.org/10.1016/j.scitotenv.2021.150306, 2022.

        Zheng, Y., Che, H., Xia, X., Wang, Y., Wang, H., Wu, Y., Tao, J., Zhao, H., An, L., Li, L., Gui, K., Sun, T., Li, X., Sheng, Z.,
        Liu, C., Yang, X., Liang, Y., Zhang, L., Liu, C., Kuang, X., Luo, S., You, Y., and Zhang, X.: Five-year observation of
735   aerosol optical properties and its radiative effects to planetary boundary layer during air pollution episodes in North China:
        Intercomparison of a plain site and a mountainous site in Beijing, Sci. Total Environ., 674, 140-158,
        https://doi.org/10.1016/j.scitotenv.2019.03.418, 2019.

        Zhu, L., Meng, Z., Zhang, F., and Markowski, P. M.: The influence of sea- and land-breeze circulations on the diurnal
        variability in precipitation over a tropical island, Atmos. Chem. Phys., 17, 13213-13232, https://doi.org/10.5194/acp-17-
740   13213-2017, 2017.